AN ARCHIVAL *Chandra* AND *XMM-Newton* SURVEY OF TYPE 2 QUASARS

JIANJUN JIA[1], ANDREW PTAK[2], TIMOTHY HECKMAN[1], AND NADIA L. ZAKAMSKA[1]
[1] Department of Physics and Astronomy, Johns Hopkins University, Baltimore, MD 21218, USA
[2] Goddard Space Flight Center, Greenbelt, MD 20771, USA

ABSTRACT

In order to investigate obscuration in high-luminosity type 2 active galactic nuclei (AGNs), we analyzed *Chandra* and *XMM-Newton* archival observations for 71 type 2 quasars detected at $0.05 < z < 0.73$, which were selected based on their [O III] $\lambda5007$ emission lines. For 54 objects with good spectral fits, the observed hard X-ray luminosity ranges from 2×10^{41} to 5.3×10^{44} erg s^{-1}, with a median of 1.1×10^{43} erg s^{-1}. We find that the means of the column density and photon index of our sample are log $N_{\rm H} = 22.9$ cm^{-2} and $\Gamma = 1.87$, respectively. From simulations using a more physically realistic model, we find that the absorbing column density estimates based on simple power-law models significantly underestimate the actual absorption in approximately half of the sources. Eleven sources show a prominent Fe Kα emission line (EW>100 eV in the rest frame) and we detect this line in the other sources through a joint fit (spectral stacking). The correlation between the Fe Kα and [O III] fluxes and the inverse correlation of the equivalent width of the Fe Kα line with the ratio of hard X-ray and [O III] fluxes is consistent with previous results for lower luminosity Seyfert 2 galaxies. We conclude that obscuration is the cause of the weak hard X-ray emission rather than intrinsically low X-ray luminosities. We find that about half of the population of optically selected type 2 quasars are likely to be Compton thick. We also find no evidence that the amount of X-ray obscuration depends on the AGN luminosity (over a range of more than three orders of magnitude in luminosity).

Key words: galaxies: active – quasars: general – X-rays: galaxies

Online-only material: color figures, figure set

1. INTRODUCTION

In the standard unification model, all active galactic nuclei (AGNs) are powered by accretion onto supermassive black holes (SMBHs), with different geometries resulting in various types of AGNs (Antonucci 1993). That is, AGNs are grossly classified by whether broad emission lines are (type 1) or are not (type 2) present in the optical and UV spectrum. In the unified model, the central accretion disk and surrounding retinue of high-velocity gas is directly visible in type 1 AGNs, while this region is blocked from a direct view by a toroidal obscuring structure in type 2 AGNs. In the local universe, low-luminosity type 2 AGNs (type 2 Seyfert galaxies) are found to be as abundant as type 1 AGNs (type 1 Seyfert galaxies) and the applicability of the unified model is well established (e.g., Hao et al. 2005). Given the strong cosmic evolution of the AGN population, the most luminous AGNs are very rare in the local universe and this population is only well characterized at high redshift. Unfortunately, the heavy obscuration by the dense gas and dust surrounding the SMBH makes type 2 AGNs much fainter than type 1 AGNs and they become difficult to discover at high redshifts. It is therefore unclear how well the standard unified model works for AGNs of the highest luminosities and at high redshifts.

Indeed, X-ray surveys have shown that the ratio of type 2 to type 1 AGNs decreases with AGN X-ray luminosity (Ueda et al. 2003; Sazonov & Revnivtsev 2004; Barger et al. 2005; Treister & Urry 2005; Akylas et al. 2006; Gilli et al. 2007; Fiore et al. 2008; Treister et al. 2008; Treister & Urry 2012), but see Dwelly & Page (2006) for different results. This anti-correlation between obscuration and luminosity is in contrast with the results from infrared (IR), radio, and optical surveys (Reyes et al. 2008, see Lawrence & Elvis 2010 for a review),

which suggests that obscured AGNs are about as common as the unobscured ones at the highest probed luminosity.

In this paper, we explore the hard X-ray and optical emission-line properties of the largest *optically selected* sample available to date of highly luminous type 2 AGNs. We then compare these properties with those of typical low-luminosity AGNs to test the unified model at high luminosity. We note that throughout the rest of our paper, we will use the term "Seyfert" to refer to low-luminosity AGNs and "quasar" to refer to high-luminosity AGNs (with a dividing line at a bolometric luminosity greater than 10^{45} erg s^{-1}).

A large sample of type 2 quasars is needed in order to test how and if the unified model applies at high luminosities. Although the central engine is hidden from view in type 2 AGNs, the strong UV radiation escaping along the polar axis of the obscuring material distribution photoionizes circumnuclear gas leading to strong, narrow high-ionization emission lines. Since this narrow-line region is at larger radii than the bulk of the obscuring material, selection based on narrow optical emission lines promises to be less biased against type 2 AGNs than hard ($E < 10$ keV) X-ray surveys (see, e.g., LaMassa et al. 2009, hereafter LM09; LaMassa et al. 2010). Since the narrow-line emission mechanism is the same for both type 1s and 2s in the standard AGN model, we can expect that the line luminosity serves as an indicator of the intrinsic luminosity of the nucleus, especially for the [O III] $\lambda5007$ emission line, which is the strongest line in the optical spectra and is not heavily contaminated by star-forming activities (Brinchmann et al. 2004; Heckman et al. 2004). When compared with the observed hard X-ray luminosity, it can also serve as a diagnostic of X-ray obscuration (Bassani et al. 1999; Gilli et al. 2010).

Zakamska et al. (2003, hereafter Z03) selected 291 type 2 quasars at redshifts $0.3 < z < 0.83$ based on their optical

emission line properties from the spectroscopic data of the Sloan Digital Sky Survey (SDSS; York et al. 2000). They found strong narrow emission lines with high-ionization line ratios but no broad emission lines in these objects and therefore identified them as type 2 quasar candidates based on [O III] $\lambda 5007$ emission-line luminosities greater than 10^8 $L_\odot$. This new method has greatly expanded the number of type 2 quasars known and it allows the properties of type 2 quasars to be studied in detail. Subsequent multi-wavelength studies (Zakamska et al. 2004, 2005, 2006; Ptak et al. 2006, hereafter P06; Vignali et al. 2006, hereafter V06) confirmed that the standard models for AGNs could give good descriptions of those optically selected type 2 quasars. Vignali et al. (2010, hereafter V10) recently studied the X-ray spectra of 25 type 2 quasars from Z03 by comparing the measured hard X-ray luminosity with the intrinsic (de-absorbed) X-ray luminosity derived from the [O III] $\lambda 5007$ and mid-IR (5.8 μm and 12.3 μm) line estimators and concluded that about half of the SDSS type 2 quasars with exceptionally high luminosities ($L_{[O III]} > 10^{9.3}$ $L_\odot$) might be Compton thick (absorbing column density $N_H > 10^{24}$ cm^{-2}). The bolometric luminosities of these quasars are difficult to determine accurately, but their high overall energetics can be gleaned from the mid-IR data (*Spitzer* and *WISE*), where obscuring material thermally re-emits much of the absorbed radiation (Zakamska et al. 2008) and monochromatic luminosities νL_ν well in excess of 10^{45} erg s^{-1} are often seen. Our estimate for bolometric luminosities based on a comparison of [O III] luminosities in type 1 and type 2 quasars is presented in Liu et al. (2009); L_{bol} is about 10^{45} erg s^{-1} at $L_{[O III]} = 10^8$ $L_\odot$ and increases approximately linearly with $L_{[O III]}$ thereafter.

By applying the same selection technique to the more recent data, a catalog containing 887 type 2 quasars from the SDSS was released by Reyes et al. (2008, hereafter R08), which expanded the original sample by a factor of four, preferentially at higher [O III] luminosities. We selected the objects covered in X-ray archival observations from this pool and investigated their X-ray properties. These objects provide the largest sample of X-ray type 2 quasars that have no bias with respect to X-ray luminosity, since they are selected on the basis of optical line emission. In this paper, we present our study of 71 type 2 quasars observed by *Chandra* and *XMM-Newton*. Section 2 describes our sample selection and data analysis. Section 3 gives the X-ray spectral analysis. We discuss our results in Section 4 and come to conclusions in Section 5. An $h = 0.7$, $\Omega_m = 0.3$, and $\Omega_\Lambda = 0.7$ cosmology is assumed throughout this paper (Spergel et al. 2003).

2. SAMPLE DESCRIPTION AND DATA ANALYSIS

By correlating those 887 optically selected type 2 quasars with the public *Chandra* (within an 8$'$ search radius) and *XMM-Newton* (within a 15$'$ search radius) archives, 71 quasars were found to be covered by *Chandra* or *XMM-Newton* or both as of 2011 February.[3] The list of the coordinates, Galactic column density, redshift, observed [O III] $\lambda 5007$ luminosity, observation ID, exposure time, observation date, and off-axis angle for each target are given in Table 1, where objects are identified by their J2000 coordinates and shortened to *hhmm+ddmm* notation elsewhere. We obtain the radio fluxes of our sample from the FIRST (Condon et al. 1998) and NVSS (Becker et al. 1995) radio catalog. By assuming a power

law ($F_\nu \propto \nu^\alpha$) with a spectral index $\alpha = -1$ at 1.4 GHz and comparing their rest-frame luminosity νL_ν(1.4 GHz) with [O III] $\lambda 5007$ luminosity, six of them are classified as radio loud (RL) sources (Xu et al. 1999; Zakamska et al. 2004): 0812+4018, 0834+5534, 1119+6004, 1347+1217, 1411+5212, and 1449+4221. Some sources were also studied and published in other papers and they are marked in the last column of Table 1. Nine objects have multiple observations and the number of total *Chandra* and *XMM* observations for the whole sample is 85. In 52 of them, the sources in our sample are the targets of observations.

The data pipeline was done using XAssist,[4] which is a software package for automatic analysis of X-ray astrophysics data. XAssist generates the light curves and can filter the raw data for flaring by its default parameter setting. However, we also checked the light curve and filtered the flaring of each observation manually. Point sources with sufficient photons are detected by XAssist automatically. In cases where sources are not detected due to insufficient counts, user-specified region files that contain the source coordinates are supplied as inputs to XAssist. CIAO (version 4.3) and XMMSAS (version 10.0.0) were called in processing *Chandra* and *XMM-Newton* data, respectively. The size of each point source extraction region was set by fitting an elliptical Gaussian function to a "stamp" image for each source, which typically results in a region size of 2$''$ (*Chandra*) and 18$''$ (*XMM-Newton*) for on-axis sources. Depending on how large the off-axis angles are, the region sizes of *Chandra* sources vary from about 4$''$ to 9$''$ and those of *XMM-Newton* sources vary from about 20$''$ to 40$''$. The fraction of energy encircled in these extraction regions from point spread function integration is above 80% (Allen et al. 2004; Read et al. 2011). Background regions are set as annuli centered on the sources, but if the source is located in a crowded region or on the edge of the detector, another circular region in the field was chosen manually for background extraction.

3. SPECTRAL ANALYSIS

We extract the spectra in the energy range of 0.3–8 keV for the *Chandra* observations. For the *XMM* ones, we used the 0.3–10 keV regime. Although the 8–10 keV emission of *XMM* data might be dominated by background and spurious spectral lines, the spectral results are nearly the same as if the 8–10 keV data were removed for the weak X-ray sources. X-ray spectral fitting is performed with XSPEC (version 12). The spectra are grouped to one count per bin and the C-statistic (Cash 1979) is used in fitting the spectra. Although the C-statistic is devised for unbinned spectra, C-statistic fitting in XSPEC performs better if the spectra are binned to at least one count per bin (Teng et al. 2005). For those sources with more than 200 photon counts collected, we group their spectra to 10 (total counts fewer than 500) or 20 (total counts more than 500) counts per bin and use the χ^2 statistic in the spectral fitting. X-ray photons are collected by three detectors on *XMM-Newton*, i.e., PN, MOS1, and MOS2. The two MOS spectra are combined and fitted simultaneously with PN spectra in XSPEC and all parameters are tied together except for a constant multiplicative factor to account for the relative flux calibration differences among the detectors. Five *XMM-Newton* sources have counts detected in only one or two of the three detectors, which are noted in the second column in Table 2. Errors are calculated at 90% significance, i.e., $\Delta\chi^2$ or $\Delta C = 2.7$ for one parameter of interest (Avni 1976).

---

[3] This work was performed using the High-Energy Astrophysics Science Archive (HEASARC), http://heasarc.gsfc.nasa.gov

[4] version 0.9993, http://xassist.pha.jhu.edu

Table 1
SDSS Type 2 AGNs Observed with *Chandra* or *XMM-Newton* or Both

Source ID J2000 Coordinates (1)	Galactic $N_{H,G}$ ($\times 10^{20}$ cm^{-2}) (2)	z (3)	$\log(L_{[O\,III]}/L_\odot)$ (4)	Observation ID (5)	Exposure (ks) (6)	Date mm/dd/yy (7)	Off-axis angle (′) (8)	Ref. (9)
SDSS J001111.97+005626.3	2.89	0.4094	8.67	*XMM*-0403760301	19.9 (P) 25.1 (M1) 25.1 (M2)	08/07/07	4.8	
SDSS J002852.86−001433.5	2.66	0.3103	8.08	*XMM*-0403160101	0.84 (P) 1.4 (M1) 1.5 (M2)	06/29/07	7.9	
SDSS J005009.81−003900.6	2.57	0.7276	10.06	*Chandra*-5694	8.0	08/28/05		b
SDSS J005621.72+003235.8	2.86	0.4840	9.25	*XMM*-0303110401	8.7 (P) 11.4 (M1) 11.4 (M2)	07/16/05		
				Chandra-7746	9.9	02/08/08		c
SDSS J012032.21−005502.0	3.69	0.6010	8.85	*Chandra*-7747	10.2	02/18/07		c
SDSS J012341.47+004435.9	3.24	0.3990	9.14	*Chandra*-6802	10.0	02/07/06		c
SDSS J013416.34+001413.6	2.91	0.5559	9.53	*Chandra*-7748	10.0	09/10/07		c
SDSS J014932.53−004803.7	2.85	0.5669	9.29	*Chandra*-7749	10.1	08/30/07		c
SDSS J015716.92−005304.8	2.58	0.4223	9.19	*Chandra*-7750	9.7	06/18/07		c
				XMM-0303110101	9.9 (P) 12.7 (M1) 12.7 (M2)	07/14/05		
SDSS J021047.01−100152.9	2.17	0.5401	9.87	*XMM*-0204340201	9.1 (P) 11.6 (M1) 11.6 (M2)	01/12/04		b,e
SDSS J030425.69+000740.9	7.05	0.5557	9.26	*XMM*-0203160201	15.4 (P) 14.9 (M1) 14.9 (M2)	07/19/04	8.1	
SDSS J031950.54−005850.6	6.05	0.6261	9.59	*Chandra*-5695	11.6	03/10/05		b
SDSS J073745.88+402146.5	6.18	0.6142	9.31	*Chandra*-7751	9.5	02/03/07		c
SDSS J075820.98+392336.0	5.22	0.2160	9.02	*XMM*-0406740101	10.89 (P) 14.22 (M1) 14.24 (M2)	10/22/06	4.1	
				XMM-0305990101	2.0 (P) 7.9 (M1) 7.9 (M2)	04/18/06	6.1	
SDSS J080154.24+441233.9	4.79	0.5561	9.64	*Chandra*-5248	9.9	11/27/03		b,e
SDSS J081253.10+401859.9	5.16	0.5512	9.39	*Chandra*-6801	10.0	12/11/05		c
SDSS J081507.42+430427.2	5.02	0.5099	9.44	*Chandra*-5696	8.3	12/27/05		b
SDSS J083454.89+553421.1	4.14	0.2414	8.69	*Chandra*-1645	9.0	10/17/01		
				Chandra-4940	96.0	01/03/04		
				XMM-0143653901	6.3 (P) 9.6 (M1) 9.6 (M2)	10/09/03	13.1	
SDSS J083945.98+384319.0	3.55	0.4246	8.60	*XMM*-0502060201	15.4 (P) 18.7 (M1) 18.7 (M2)	10/16/07	10.8	f
SDSS J084041.08+383819.8	3.45	0.3132	8.45	*XMM*-0502060201	15.4 (P) 18.8 (M1) 18.8 (M2)	10/16/07		f
SDSS J084234.94+362503.1	3.41	0.5615	10.02	*Chandra*-532	19.7	10/21/99	5.4	b,e
SDSS J085331.39+175347.3	2.94	0.1865	8.92	*XMM*-0305480301	23.3 (P) 68.6 (M1) 68.4 (M2)	10/28/05	11.4	
SDSS J085554.47+370900.4	2.93	0.3567	8.84	*Chandra*-6807	10.5	02/17/06	4.93	
SDSS J090037.09+205340.2	3.39	0.2357	8.98	*Chandra*-10463	41.2	02/24/09		
				Chandra-7897	9.1	12/23/06	1.3	
				XMM-0402250701	9.9 (P) 15.7 (M1) 15.7 (M2)	04/13/07		
SDSS J091345.48+405628.2	1.82	0.4409	10.33	*Chandra*-509	9.2	11/03/99		
				Chandra-10445	76.2	01/06/09		
				XMM-0147671001	10.2 (P) 13.5 (M1) 13.5 (M2)	04/24/03	1.1	
SDSS J092014.10+453157.3	1.51	0.4025	9.15	*Chandra*-6803	10.2	03/05/06		c
SDSS J092152.45+515348.1	1.42	0.5877	9.41	*Chandra*-7752	10.2	09/27/07		c
SDSS J092318.06+010144.8	3.32	0.3873	8.77	*XMM*-0551201001	23.1 (P) 26.7 (M1)	11/06/08		f
SDSS J092438.24+302837.1	1.94	0.2727	8.80	*XMM*-0553440601	4.4 (P) 6.5 (M1)	11/22/08	10.3	
SDSS J093952.74+355358.0	1.43	0.1366	8.75	*XMM*-0021740101	26.6 (P) 33.9 (M1) 33.9 (M2)	10/27/01		
SDSS J094506.39+035551.1	3.71	0.1559	8.60	*XMM*-0201290301	24.9 (P) 37.0 (M1) 37.0 (M2)	05/19/04	10.0	
SDSS J100327.93+554153.9	0.775	0.1460	8.24	*XMM*-0110930201	17.1 (P) 24.5 (M1) 24.5 (M2)	04/13/01	13.2	
SDSS J102229.00+192939.0	2.36	0.4063	9.13	*Chandra*-4907	7.3	03/31/05		
SDSS J102746.03+003205.0	4.47	0.6137	9.46	*Chandra*-7883	10.0	01/13/07		c
SDSS J103408.59+600152.2	0.69	0.0511	8.81	*XMM*-0306050701	8.8 (P) 11.4 (M1) 11.4 (M2)	04/04/05	1.2	
SDSS J103456.40+393940.0	1.47	0.1507	8.91	*XMM*-0506440101	11.9 (P) 15.0 (M1) 15.0 (M2)	05/01/02	4.6	
SDSS J103951.49+643004.2	1.18	0.4018	9.43	*Chandra*-7753	10.0	02/04/07		c
SDSS J104426.70+063753.8	2.82	0.2104	8.16	*XMM*-0405240901	24.0 (P) 31.0 (M1) 31.0 (M2)	06/05/07	5.5	
SDSS J110621.96+035747.1	4.58	0.2424	9.01	*Chandra*-6806	10.2	02/02/06		
SDSS J111907.01+600430.8	0.71	0.2642	8.28	*XMM*-0502780201	9.6 (P) 13.5 (M1) 13.5 (M2)	05/20/07		
SDSS J113153.75+310639.7	1.96	0.3727	8.52	*XMM*-0102040201	17.2 (M1) 23.3 (M2)	11/22/00	12.1	
SDSS J114544.99+024126.9	2.21	0.1283	8.19	*XMM*-0551022701	13.8 (P)	06/15/08	8.0	
SDSS J115138.24+004946.4	2.26	0.1951	8.40	*Chandra*-7735	4.7	07/09/07		
SDSS J115314.36+032658.6	1.89	0.5748	9.64	*Chandra*-5697	8.3	04/10/05		b
SDSS J115718.35+600345.6	1.65	0.4903	9.61	*Chandra*-5698	7.1	06/06/06		b
SDSS J121839.40+470627.7	1.17	0.0939	8.56	*XMM*-0203270201	14.2 (P) 33.3 (M1) 35.0 (M2)	06/01/04	6.0	d
SDSS J122656.40+013124.3	1.84	0.7321	9.8	*XMM*-0110990201	21.3 (P) 28.6 (M1) 28.6 (M2)	06/23/01	5.0	a,e
SDSS J122709.84+124854.5	2.64	0.1945	8.5	*XMM*-0210270101	22.0 (P) 26.2 (M1) 26.2 (M2)	12/19/04	3.8	
				Chandra-5912	32.6	03/09/05	4.2	
				Chandra-9509	25.8	04/14/08	6.7	
				Chandra-9510	25.2	04/14/08	7.5	
SDSS J122845.74+005018.7	1.88	0.5750	9.28	*Chandra*-7754	9.5	03/12/07		c
SDSS J123215.81+020610.0	1.80	0.4807	9.62	*Chandra*-4911	9.7	04/21/05		b,e
SDSS J123843.02+092744.0	1.87	0.0829	8.51	*XMM*-0504100601	17.4 (P) 21.3 (M1) 21.3 (M2)	12/09/07	1.7	d
SDSS J124302.48+122022.8	2.34	0.4857	9.09	*Chandra*-11322	10.6	02/28/10	3.4	

Table 1
(Continued)

Source ID J2000 Coordinates (1)	Galactic $N_{\rm H,G}$ ($\times 10^{20}$ cm^{-2}) (2)	z (3)	$\log(L_{\rm [O\,III]}/L_\odot)$ (4)	Observation ID (5)	Exposure (ks) (6)	Date mm/dd/yy (7)	Off-axis angle (′) (8)	Ref. (9)
SDSS J124337.34−023200.2	2.03	0.2814	8.88	*Chandra*-6805	10.2	04/25/06		
SDSS J130128.76−005804.3	1.59	0.2455	9.12	*Chandra*-6804	10.2	05/30/06		
SDSS J131104.36+272813.4	0.98	0.2398	8.46	*XMM*-0021740201	40.3 (P) 43.7 (M1) 43.7 (M2)	12/12/02		
				Chandra-12735	8.0	11/17/10		
SDSS J132419.88+053704.6	2.26	0.2027	8.49	*XMM*-0200660301	10.7 (P) 10.0 (M1) 10.2 (M2)	07/11/04	1.7	
SDSS J132946.20+114009.3	1.93	0.5596	9.36	*XMM*-0041180801	15.6 (P) 22.3 (M1) 22.3 (M2)	12/30/01	7.8	
SDSS J133735.02−012815.7	2.41	0.3292	8.71	*XMM*-0502060101	2.4 (M2)	07/11/07		f
SDSS J134733.36+121724.3	1.90	0.1204	8.65	*Chandra*-836	28.0	02/24/00		
SDSS J141120.52+521210.0	1.33	0.4617	8.41	*Chandra*-2254	92.1	05/18/01		
SDSS J143027.66−005614.9	3.35	0.3177	8.42	*XMM*-0502060301	1.4 (P) 5.0 (M1) 5.0 (M2)	08/03/07		f
SDSS J143156.38+325137.7	1.07	0.4198	9.52	*Chandra*-10457	34.6	10/30/08	6.0	
SDSS J144642.29+011303.0	3.55	0.7259	9.54	*Chandra*-7755	10.2	03/22/07		c
SDSS J144920.72+422101.3	1.53	0.1784	8.85	*Chandra*-5717	4.4	10/04/05		
SDSS J150719.93+002905.1	4.48	0.1819	8.98	*XMM*-0305750801	10.5 (P) 13.4 (M1) 13.4 (M2)	07/20/05	1.1	
SDSS J151711.47+033100.2	3.78	0.6128	9.10	*Chandra*-7756	10.0	03/28/07		c
SDSS J160641.42+272556.9	3.89	0.5411	9.44	*XMM*-0304070701	2.2 (M1) 1.9 (M2)	07/29/05	9.2	
SDSS J164131.73+385840.9	1.16	0.5957	10.04	*XMM*-0204340101	12.2 (P) 16.8 (M1) 17.1 (M2)	08/20/04		b,e
SDSS J171350.32+572954.9	2.48	0.1128	8.95	*XMM*-0305750401	6.2 (P) 8.7 (M1) 8.7 (M2)	06/23/05		
SDSS J235818.86−000919.4	3.25	0.4025	9.27	*XMM*-0303110301	1.9 (P) 5.8 (M1) 5.7 (M2)	12/04/05		
				XMM-0303110801	6.9 (P) 9.5 (M1) 9.5 (M2)	06/20/06		b
SDSS J235831.16−002226.5	3.29	0.6277	9.68	*Chandra*-5699	6.3	08/08/05		b

Notes. Column 1: J2000 coordinates; Column 2: Galactic column density calculated by the HEAsoft $N_{\rm H}$ tool; Column 3: redshift; Column 4: [O III] λ5007 line luminosity in units of solar (from Reyes et al. (2008)); Column 5: *Chandra* and *XMM-Newton* observation ID; Column 6: exposure times after filtering in units of ks (for *XMM-Newton* observations, the exposure times are listed separately for the PN (P) and MOS1,2 (M1,2) instruments); Column 7: date of observation; Column 8: separation from the center of field of view in units of arcminutes; Column 9: references that have the source included: (a) Vignali et al. (2004; V04); (b) Vignali et al. (2006; V06); (c) Vignali et al. (2010; V10); (d) LaMassa et al. (2009; LM09); (e) Ptak et al. (2006; P06); (f) Lamastra et al. (2009; L09).

The X-ray spectra of obscured (type 2) AGNs are complicated and usually consist of multiple components: power-law, thermal, scattering, reflection, and emission lines (see Turner et al. 1997; Risaliti 2002; Ptak et al. 2006; LaMassa et al. 2009). Thus, no single model could fit the spectra well in all cases. We carry out the spectral fit with XSPEC using several spectral models.

1. *Single absorber power law.* Initially, the spectrum is fit as a power-law continuum absorbed by the Galactic column density ($N_{\rm H,G}$) and an intrinsic redshifted absorption column density ($N_{\rm H}$). This model results in three free parameters: the column density $N_{\rm H}$, the photon index Γ, and the power-law normalization. The Galactic neutral hydrogen column density $N_{\rm H,G}$ is a fixed parameter (Dickey & Lockman 1990), which is calculated from the HEAsoft $N_{\rm H}$ tool. However, in some cases, we fixed the photon index at $\Gamma = 1.7$ (which is a typical value for AGNs; Nandra et al. 2005) if it is unconstrained, i.e., the errors exceeded reasonable bounds.

2. *Double-absorber power law.* In some cases, a single absorbed power law cannot model the data accurately and a two-absorber model could be an approximation to the case of X-ray photons being scattered into the line of sight (Turner et al. 1997; Ptak et al. 2006; LaMassa et al. 2009). We applied this model to 17 sources and considered this approach to be the best-fitting model. The photon indices of both power-law components are tied together when fitting the spectra. However, tying the photon indices in the case of SDSS J1034+6001 results in a very large χ^2 and we thus use two different indices in fitting its spectrum. For those sources, which have very small values for $N_{\rm H,1}$ (lower than

$N_{\rm H,G}$) during spectral fitting, we then fixed their values to $N_{\rm H,G}$.

3. *Absorbed power law plus Gaussian Fe Kα line.* Eleven objects show visually detected Fe Kα emission lines and a Gaussian component was added to the best-fitting power-law continuum. We initially fixed the line energy $E_{\rm line}$ at 6.4 keV (in the source rest frame) and the line width (σ) at 0.01 keV ($\sim$10% of the instrumental line resolution for *Chandra* and *XMM-Newton*). In XSPEC, we first ignore the photon counts in the energy range of 5–7 keV to get the power-law index of the continuum, and then notice them to fit the emission line around 6.4 keV. The line energy of 0834+5534 is around 6.7 keV instead of 6.4 keV.

We list the photon counts, the column densities, and the photon indices of the best-fitting spectral fits for 54 sources that have enough photon counts to result in a moderate quality spectral fit in Table 2, as well as the derived observed and intrinsic (de-absorbed) 2–10 keV luminosities and the ratios of the X-ray to [O III] luminosity. For the cases with double power-law fits, we also list the ratio of the normalization of both power-law components. Some quasars have very small column densities in the spectral fits and we use the upper limit instead in Table 2. The spectral plots of each quasar are shown in Figure 1. For those with multiple observations in either *Chandra* or *XMM* or both, we also report in Table 2 the column density, photon index, and χ^2 from the simultaneous fits of all spectral data and we use these values in following discussions. Discrepancies between each individual observation are discussed in Appendix B.

There are 17 sources whose observations are dominated by background. The photon counts are too low to constrain the

Table 2
X-Ray Spectral Properties of SDSS Type 2 AGNs

Source ID	Total Counts and Estimated Background Counts	$N_{H,1}$ $(10^{22}$ cm$^{-2})$	Γ	$N_{H,2}$ $(10^{22}$ cm$^{-2})$	PL1/PL2	χ^2/dof or c-stat/dof	L_X $(10^{44}$ erg s$^{-1})$	$L_{X,in}$ $(10^{44}$ erg s$^{-1})$	$L_X/L_{[O\,III]}$	$L_{X,in}/L_{[O\,III]}$	Compton Thick
(1)	(2)	(3)	(4)	(5)	(6)	(7)	(8)	(9)	(10)	(11)	(12)
0011+0056	77(62.6)/.../57(31.3)	<2.70	$0.60^{+1.17}_{-1.15}$			123.3/122	0.031	0.031	1.7	1.7	✓
0050−0039	45(0.4)	$35.5^{+34.7}_{-26.0}$	$1.73^{+1.86}_{-1.66}$			51.0/39	1.83	7.21	4.2	16.4	✓
0056+0032	25(18.4)/16(8.8)/18(10.5)	<0.96	$1.84^{+2.46}_{-1.41}$			69.3/54	0.04	0.04	0.59	0.59	✓
0123+0044	161(0.3)	$6.92^{+3.28}_{-2.80}$	$0.69^{+0.63}_{-0.61}$			115.1/128	1.81	2.44	34.2	46.0	
0157−0053	23(0.2)	$N_{H,G}$	$2.03^{+1.57}_{-1.56}$	$48.5^{+106.5}_{-28.0}$	0.011	10.2/19	0.30	1.63	5.0	27.4	
	351(322.2)/72(47.6)/83(46.3)	<0.11	$1.64^{+0.81}_{-0.63}$			443.8/439	0.13	0.13	2.2	2.2	
0210−1001	189(31.2)/78(8.1)/77(8.5)	$3.03^{+2.06}_{-1.42}$	$0.89^{+0.38}_{-0.35}$			325.9/312	1.81	2.0	6.3	7.0	
0304+0007	.../29(18.2)/28(20.3)	$43.4^{+73.2}_{-20.4}$	$2.10^{+2.07}_{-3.39}$			58.1/51	0.31	1.63	4.4	23.0	
0758+3923	90(43.7)/20(8.9)/20(9.3)	<0.24	$1.38^{+0.96}_{-0.70}$			8.6/8	0.02	0.02	0.44	0.44	✓
	85(69.4)/45(38.3)/46(38.3)	$0.26^{+0.42}_{-0.21}$	$2.04^{+2.82}_{-1.15}$			142.1/164	0.07	0.07	1.5	1.5	
		<0.25	$1.68^{+0.94}_{-0.71}$			21.3/29					
0801+4412	47(2.4)	$N_{H,G}$	$1.08^{+1.28}_{-1.29}$	$40.8^{+38.8}_{-24.9}$	0.035	44.9/40	0.93	2.90	5.5	17.2	
0812+4018	201(0.8)	$0.93^{+0.45}_{-0.42}$	$1.91^{+0.37}_{-0.36}$			104.9/125	1.56	1.70	16.4	18.0	
0834+5534	174(57.9)	$0.054^{+0.048}_{-0.043}$	$1.64^{+0.36}_{-0.32}$			101.9/113	0.17	0.17	9.0	9.0	
	2967(3.0)	$0.11^{+0.03}_{-0.03}$	$2.09^{+0.10}_{-0.10}$			107.9/100	0.21	0.22	11.1	11.2	
	2514(238.8)/1079(74.5)/1110(69.9)	$0.12^{+0.02}_{-0.02}$	$2.24^{+0.10}_{-0.09}$			236.2/200	2.67	2.71	142	144	
		$0.12^{+0.02}_{-0.03}$	$2.12^{+0.11}_{-0.10}$			128.6/122					
0839+3843	363(137.6)/133(37.9)/111(41.5)	$2.01^{+1.57}_{-1.05}$	$1.21^{+0.45}_{-0.39}$			54.6/55	1.36	1.56	89.0	102.0	
0840+3838	91(64.7)/30(21.9)/29(20.9)	<0.38	$2.08^{+1.68}_{-1.17}$			130.4/137	0.008	0.008	0.71	0.71	✓
0853+1753	134(28.3)/169(52.9)/124(15.7)	$N_{H,G}$	$2.42^{+0.44}_{-0.38}$	$55.7^{+14.9}_{-11.7}$	0.007	299.8/364	0.08	0.62	2.5	19.4	✓
0855+3709	26(1.6)	$3.27^{+4.66}_{-3.05}$	$1.14^{+1.47}_{-1.29}$			26.6/23	0.23	0.28	8.6	11.3	
0900+2053	2017(2.0)	$N_{H,G}$	$1.83^{+0.25}_{-0.15}$	$37.4^{+10.4}_{-7.8}$	0.066	73.1/76	1.10	3.52	30.0	96.0	
	336(0.3)	$N_{H,G}$	$1.54^{+0.52}_{-0.46}$	$52.9^{+50.1}_{-26.6}$	0.110	11.5/12	1.21	4.42	33.0	120.5	
	7871(23.6)/3705(7.4)/3098(9.3)	$0.12^{+0.02}_{-0.02}$	$2.30^{+0.09}_{-0.09}$	$80.0^{+33.0}_{-27.5}$	0.265	567.7/535	2.50	9.14	68.2	249.3	
		$N_{H,G}$	$1.81^{+0.15}_{-0.11}$	$37.3^{+7.9}_{-5.8}$	0.075	87.5/91					
0913+4056	250(50.0)	$0.08^{+0.04}_{-0.03}$	$2.24^{+0.69}_{-0.53}$	$29.2^{+31.6}_{-13.3}$	0.113	135.9/139	1.74	5.07	2.1	6.1	✓
	2298(2.3)	$N_{H,G}$	$1.93^{+0.19}_{-0.17}$	$62.1^{+28.2}_{-19.7}$	0.142	101.8/86	2.30	9.28	2.8	11.2	
	6259(275.4)/2470(86.5)/2574(75.6)	$0.09^{+0.03}_{-0.03}$	$1.98^{+0.07}_{-0.13}$	$78.0^{+60.6}_{-51.4}$	1.233	455.9/423	9.61	16.0	35.1	58.4	
			$1.89^{+0.17}_{-0.12}$	$58.3^{+22.9}_{-13.0}$	0.158	134.6/108					
0920+4531	17(2.6)	<0.31	$1.38^{+1.32}_{-0.93}$			17.1/15	0.04	0.04	0.72	0.72	✓
0923+0101	171(120.2)/38(31.5)/24(25.4)	<0.08	1.7			188.1/205	0.026	0.026	1.1	1.1	✓
0924+3028	53(38.2)/24(6.2)/...	$N_{H,G}$	$1.50^{+3.19}_{-2.20}$	$35.3^{+53.2}_{-32.7}$	0.006	88.9/67	0.28	0.93	11.6	38.5	
0939+3553	782(136.9)/536(94.3)/544(97.4)	$N_{H,G}$	$1.73^{+0.26}_{-0.24}$	$11.4^{+4.6}_{-3.0}$	0.148	108.6/86	0.19	0.32	8.9	14.9	
0945+0355	.../40(31.8)/34(25.5)	<0.55	1.7			62.8/65	0.015	0.015	0.96	0.96	
1003+5541	141(120.7)/103(91.7)/107(94.4)	<1.55	$0.80^{+2.02}_{-1.33}$			277.8/321	0.04	0.04	6.0	6.0	
1022+1929	21(4.5)	$1.06^{+2.18}_{-0.84}$	$1.50^{+1.40}_{-1.38}$			25.0/17	0.11	0.12	2.1	2.3	
1034+6001[a]	560(49.8)/124(9.3)/123(12.4)	$0.06^{+0.18}_{-0.06}$	$1.75^{+1.81}_{-1.22}$	$26.3^{+42.1}_{-26.3}$	0.403	84.3/68	0.009	0.02	0.39	0.87	✓
1034+3939	859(280.9)/307(113.6)/299(120.8)	$N_{H,G}$	$2.89^{+0.25}_{-0.23}$	$77.8^{+82.2}_{-52.6}$	0.010	145.1/133	0.02	0.21	0.5	5.0	✓
1039+6430	11(4.3)	<0.32	1.7			12.2/10	0.02	0.02	0.19	0.19	✓
1044+0637	263(133.9)/100(42.2)/110(52.3)	$N_{H,G}$	$2.54^{+1.72}_{-1.44}$	$87.1^{+50.9}_{-33.9}$	0.002	42.0/40	0.07	0.96	12.4	170.1	
1106+0357	26(3.6)	<0.20	$0.81^{+0.58}_{-0.53}$			16.3/20	0.046	0.046	1.2	1.2	✓
1119+6004	1301(1010.9)/326(215.8)/266(167.0)	<0.02	$1.99^{+0.34}_{-0.31}$			129.9/90	0.10	0.10	13.3	13.3	
1131+3106	.../.../54(49.9)	<1.44	$2.56^{+4.88}_{-1.54}$			38.4/51	0.03	0.03	2.0	2.0	✓
1145+0241	146(100.0)/.../...	<0.05	$3.12^{+1.30}_{-1.26}$			153.7/127	0.004	0.004	0.71	0.71	✓
1153+0326	91(2.8)	<0.43	$0.73^{+0.42}_{-0.33}$			87.5/74	1.30	1.30	7.7	7.7	
1218+4706	90(38.8)/144(41.6)/170(50.5)	$N_{H,G}$	$2.55^{+0.39}_{-0.30}$	$80.2^{+55.8}_{-41.0}$	0.011	21.8/31	0.006	0.02	0.4	1.7	✓
1226+0131	221(27.4)/186(32.6)/216(50.0)	$2.42^{+0.70}_{-0.61}$	$1.69^{+0.30}_{-0.24}$			96.9/93	3.24	3.93	13.4	16.2	
1227+1248	221(141.9)/62(26.2)/50/(37.0)	$N_{H,G}$	$2.26^{+0.84}_{-0.66}$	$76.7^{+81.3}_{-41.4}$	0.007	276.1/303	0.04	0.41	3.2	34.2	✓
	66(0)	$20.6^{+11.7}_{-8.3}$	$1.86^{+1.02}_{-1.13}$			58.2/59	0.07	0.18	5.8	15	
	27(2.0)	$26.6^{+35.7}_{-19.1}$	$2.33^{+2.34}_{-2.27}$			20.0/23	0.04	0.13	3.3	10.8	
	22(0)	$6.66^{+9.44}_{-3.85}$	1.7			16.4/20	0.03	0.04	2.5	3.3	
		$19.9^{+10.5}_{-8.6}$	$1.78^{+0.96}_{-0.96}$			98.0/103					
1228+0050	54(3.3)	$13.2^{+12.1}_{-8.9}$	$1.55^{+0.67}_{-1.38}$			51.3/45	1.17	2.21	15.8	30.6	
1232+0206	12(2.8)	$7.45^{+13.8}_{-5.52}$	$2.11^{+2.01}_{-1.62}$			17.8/13	0.09	0.33	0.14	0.87	✓
1238+0927	1616(150.3)/540(57.2)/545(53.4)	$N_{H,G}$	$2.26^{+0.29}_{-0.23}$	$45.3^{+6.3}_{-4.7}$	0.004	313.0/246	0.18	1.00	14.5	80.6	
1243−0232	11(0.6)	<2.84	1.7			12.8/8	0.007	0.008	0.16	1.17	✓
1301−0058	50(4.0)	$11.1^{+8.4}_{-5.9}$	$2.16^{+1.59}_{-1.40}$			74.1/42	0.18	0.39	3.5	7.8	✓
1311+2728	385(125.5)/102(33.3)/101(33.4)	<0.11	$2.48^{+0.58}_{-0.20}$			416.7/434	0.015	0.015	1.4	1.4	✓

Table 2
(Continued)

Source ID (1)	Total Counts and Estimated Background Counts (2)	$N_{H,1}$ (10^{22} cm^{-2}) (3)	Γ (4)	$N_{H,2}$ (10^{22} cm^{-2}) (5)	PL1/PL2 (6)	χ^2/dof or c-stat/dof (7)	L_X (10^{44} erg s^{-1}) (8)	$L_{X,in}$ (10^{44} erg s^{-1}) (9)	$L_X/L_{[O\,III]}$ (10)	$L_{X,in}/L_{[O\,III]}$ (11)	Compton Thick (12)
	19(0)	$0.21^{+0.27}_{-0.18}$	$2.55^{+2.35}_{-1.24}$			5.6/13	0.01	0.01	0.9	0.9	
1324+0537	61(42.8)/20(15.3)/50(29.2)	<0.12	$1.69^{+1.68}_{-0.86}$			128.1/123	0.02	0.02	1.7	1.7	✓
1329+1140	344(254.9)/131(111.6)/140(123.8)	$0.25^{+0.17}_{-0.11}$	$2.73^{+1.47}_{-0.94}$			426.9/472	0.13	0.14	1.5	1.6	
1337−0128	.../.../12(5.0)	<2.02	1.7			19.6/10	0.065	0.065	3.3	3.3	
1347+1217	1110(5.6)	$0.22^{+0.11}_{-0.10}$	$1.59^{+0.32}_{-0.32}$	$4.43^{+0.94}_{-0.85}$	0.049	360.7/378	0.35	0.47	17.1	20.6	
1411+5212	6159(43.1)	$N_{H,G}$	$3.56^{+0.11}_{-0.05}$	$19.52^{+1.59}_{-1.37}$	0.058	416.5/238	2.35	10.22	238.0	1036.0	
1430−0056	15(9.5)/6(8.3)/10(6.1)	<0.23	1.7			38.5/28	0.023	0.023	2.3	2.3	✓
1431+3251	124(1.5)	$39.9^{+30.4}_{-16.5}$	$1.85^{+1.71}_{-1.02}$			9.1/9	0.69	3.01	5.4	23.6	✓
1449+4221	31(0.5)	$N_{H,G}$	1.7	$17.23^{+15.9}_{-8.0}$	0.040	43.2/33	0.17	0.38	6.2	13.9	
1507+0029	754(492.4)/162(90.7)/161(84.2)	$6.04^{+9.56}_{-4.79}$	$2.51^{+1.11}_{-1.23}$	$66.8^{+32.7}_{-27.9}$	0.052	96.4/100	0.23	2.18	6.3	59.2	
1641+3858	991(68.4)/438(25.0)/450(25.7)	$2.28^{+0.48}_{-0.41}$	$1.34^{+0.14}_{-0.14}$			210.9/174	5.31	6.20	12.6	14.7	
1713+5729	314(241.2)/71(45.2)/82(46.9)	<0.03	$2.53^{+0.42}_{-0.43}$			75.1/43	0.008	0.008	0.26	0.26	✓
2358−0009	39(34.6)/22(14.9)/14(13.9)	<1.30	$2.27^{+0.48}_{-0.23}$			58.9/72	0.033	0.033	0.45	0.45	✓
	42(27.9)/12(7.4)/15(10.5)	<0.27	$3.68^{+5.60}_{-1.98}$			55.9/63	0.015	0.015	0.06	0.06	
		<0.37	$2.24^{+2.32}_{-1.17}$			114.8/136					

Notes. Column 1: Source ID in *hhmm+ddmm* notation; Column 2: total and background photon counts for each detector; Column 3: column density of the first absorber; Column 4: photon index of the power law; Column 5: column density of the second absorber; Column 6: the ratio of power-law norms; Column 7: χ^2 or C-statistic and degrees of freedom; Column 8: observed hard X-ray (2–10 keV in rest frame) luminosity derived from spectral fit; Column 9: intrinsic hard X-ray luminosity after correction for absorption; Column 10: observed X-ray to [O III] luminosity ratio; Column 11: intrinsic X-ray to [O III] luminosity ratio; Column 12: Compton thick or not (see Section 4.6).
[a] SDSS J1034+6001: The photon index of the two power-law components are not tied together in the spectral fits. The other photon index is $3.01^{+1.51}_{-0.58}$.

Table 3
X-Ray Counts, Count Rates, and 3σ Upper Limits of Marginally Detected AGNs

Source ID (1)	Observed Counts (2)	S_{max} (3)	Count Rates (4)	$f_{2-10\,keV}$ (5)	$L_{2-10\,keV}$ (6)	Compton Thick (7)
0028−0014[a]	12 (15.2) (M2)	12.3	0.0081	5.3×10^{-13}	1.2×10^{44}	
0120−0055	2 (0.3)	9.7	0.0010	4.1×10^{-14}	3.9×10^{43}	✓
0134+0014	3 (1.3)	10.4	0.0010	2.3×10^{-14}	1.2×10^{43}	✓
0149−0048	1 (1.2)	7.3	0.0007	1.6×10^{-14}	1.3×10^{43}	✓
0319−0058	9 (2.9)	18.0	0.0016	3.5×10^{-14}	3.6×10^{43}	✓
0737+4021	3 (0.2)	11.5	0.0012	2.6×10^{-14}	2.6×10^{43}	✓
0815+4304	2 (0.3)	9.7	0.0012	2.7×10^{-14}	1.8×10^{43}	✓
0842+3625	8 (2.2)	17.3	0.0009	4.4×10^{-14}	3.6×10^{43}	✓
0921+5153	1 (0.7)	7.5	0.0007	1.6×10^{-14}	1.4×10^{43}	✓
1027+0032	6 (2.0)	14.4	0.0015	4.3×10^{-14}	4.3×10^{43}	✓
1151+0049	5 (2.4)	12.5	0.0027	8.0×10^{-14}	7.1×10^{42}	
1157+6003	4 (3.3)	10.4	0.0015	3.5×10^{-14}	2.1×10^{43}	✓
1243+1220	6 (1.9)	14.5	0.0014	3.6×10^{-14}	2.2×10^{43}	✓
1446+0113	10 (3.7)	18.6	0.0019	3.7×10^{-14}	5.2×10^{43}	
1517+0331	8 (4.4)	15.1	0.0015	3.2×10^{-14}	3.1×10^{43}	
1606+2725[a]	15 (15.2) (M1)	15.1	0.0068	3.6×10^{-13}	2.7×10^{44}	✓
2358−0022	5 (2.2)	12.7	0.0020	4.6×10^{-14}	4.8×10^{43}	✓

Notes. Column 1: Source ID in *hhmm+ddmm* notation; Column 2: observed total counts and the estimated mean background counts (in parentheses); Column 3: upper limit of source counts at the 3σ level; Column 4: count rates; Column 5: flux in the 2–10 keV range; Column 6: observed hard X-ray (2–10 keV in the rest frame) luminosity; Column 7: Compton thick or not (see Section 4.6). Values reported in columns 4, 5, and 6 are upper limits.
[a] Photons are obtained by three detectors on *XMM-Newton* for 0028−0014 and 1606+2725. We chose the lowest flux upper limit among PN/MOS1/MOS2 as the flux limit.

spectral parameters in spectral fitting. Therefore, we calculate the upper limit of the 2–10 keV flux at a 3σ level. We assume that their spectra are an absorbed power law with $\Gamma = 1.7$ and $N_H = 10^{23}$ cm^{-2}, which is close to the mean value of the column densities given in Table 2 (see Section 4.1)[5]. The 3σ upper limit of the 2–10 keV photon count rates are calculated by using the Bayesian statistical method of Kraft et al. (1991). We

determined the count rate to flux conversion coefficient using XSPEC and multiply it by the count rate upper limit to calculate the 2–10 keV flux upper limit. The detected counts, the source count upper limits, and the associated upper limits on the count rates, fluxes, and luminosities are listed in Table 3. Table 4 lists the Gaussian fit parameters of the iron lines as well as the equivalent width (EW) and line luminosity. The change in χ^2 if we remove the Gaussian component from the spectral fit is also listed in Table 4 to show how significant this emission line is.

---

[5] The low photon counts of 0028−0014 and 1606+2725 might be due to their short effective exposure time rather than heavy absorption. However, we use the same assumption as the other 15 sources to estimate their upper limit fluxes.
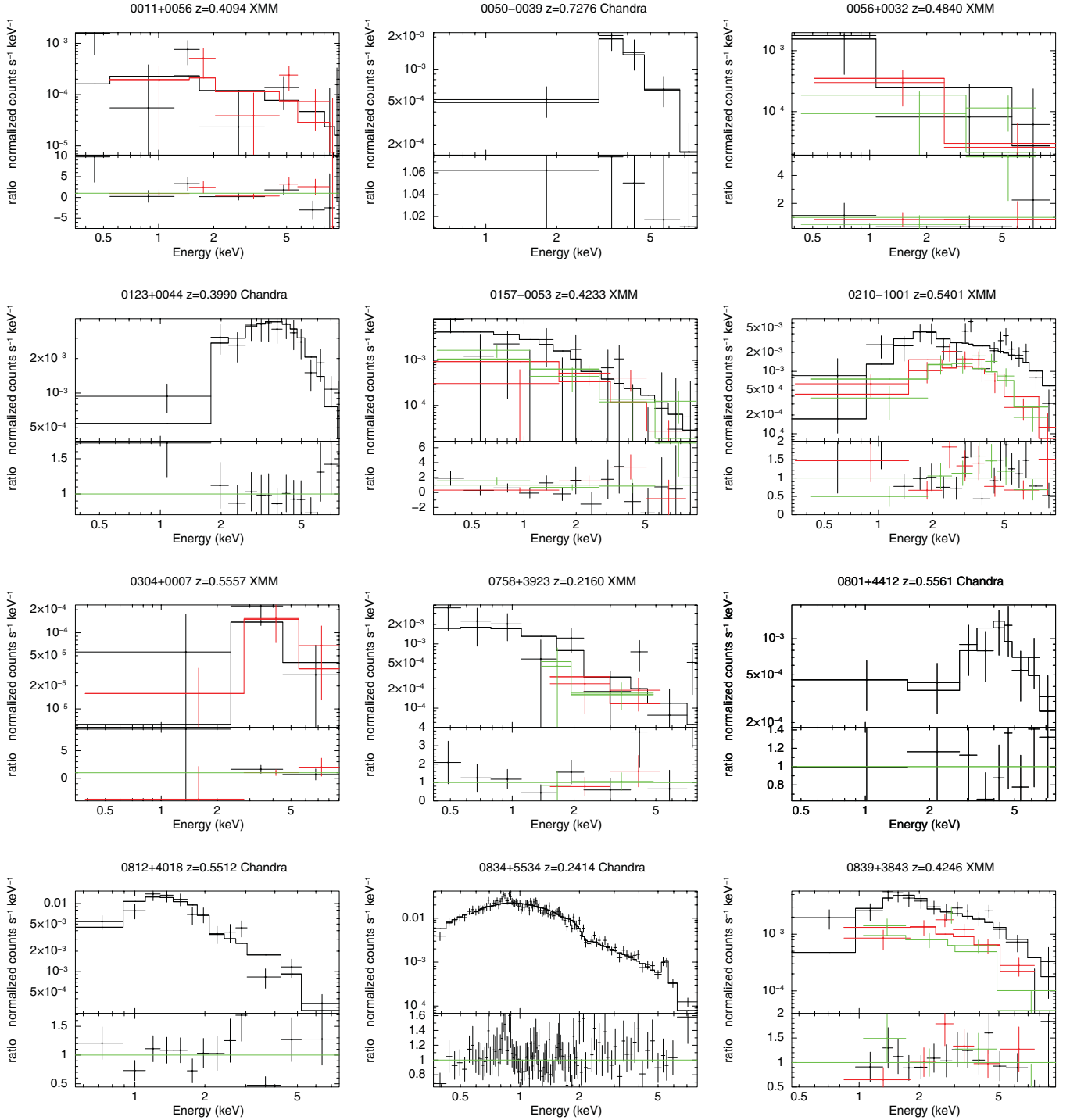
Figure 1. Spectral plots of the best fits of each source. The ratio of the data divided by the folded model is shown in the bottom panels. The spectral data in some plots are rebinned for display purposes.

(A color version and the complete figure set (54 images) are available in the online journal.)

4. RESULTS AND DISCUSSIONS

4.1. Column Density and Photon Index Distribution

Of our 71 quasars, at least crude spectral fitting is possible for 54. For these, we find that the mean power-law index is $\Gamma = 1.87 \pm 0.65$ using the best-fitting results in Table 2 (those with photon indices fixed at 1.7 are excluded), where the error bar is the standard deviation of the power-law indices of the sample neglecting the individual fitting errors. In the case that

there are multiple observations for one object, we use the values of the simultaneous joint fit instead. Multiple observations may give different fluxes or observed luminosities due to AGN variability. However, the spectral shape between different observations does not change significantly (see Figure 13). Thus, it is safe for us to use the photon index derived from the simultaneous joint fit. The six sources also claimed as RL sources have a mean photon index of 2.14 compared with 1.83 for the remainder of the sample. Therefore, their presence does
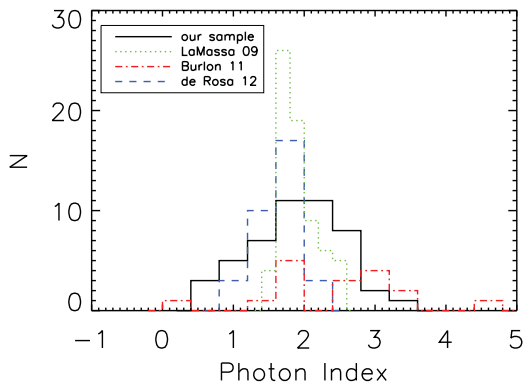
Figure 2. Histograms of photon indices of the absorbed power-law spectral fits of our sample (solid black line). We also show the sample of type 2 AGNs from the *SWIFT*-BAT survey (Burlon et al. 2011, green dotted line), the sample of hard X-ray selected obscured AGNs from *INTEGRAL* (de Rosa et al. 2012, dashed blue line), and the sample of optically selected local Seyfert 2s (LaMassa et al. 2009, dot-dashed red line) for comparison.

(A color version of this figure is available in the online journal.)

Table 4
Fe Kα Features of the AGNs with a Visually Detected Iron Emission Line

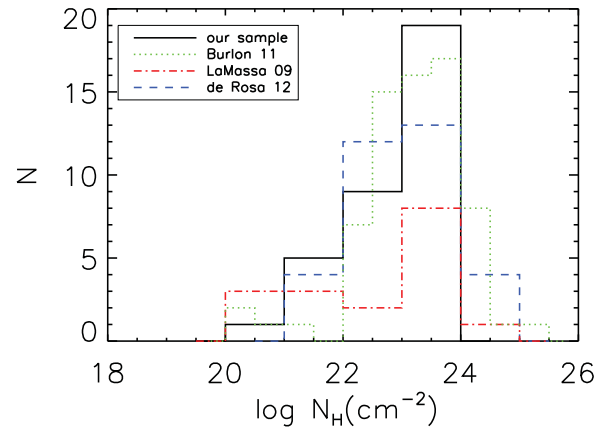| Source ID	$E_{\rm line}$[a]	EW[a] (eV)	$L_{\rm Fe}$ (10^{42} erg s^{-1})	χ^2/dof	$\Delta\chi^2$
0834+5534	$6.75^{+0.14}_{-0.11}$	598^{+425}_{-308}	$1.64^{+1.17}_{-0.84}$	107.9/100	18.3
0900+2053	$6.34^{+0.08}_{-0.07}$	$183^{+81.1}_{-78.5}$	$4.36^{+1.93}_{-1.87}$	73.1/76	15.6
0913+4056	$6.44^{+0.10}_{-0.10}$	457^{+473}_{-289}	$17.6^{+18.2}_{-11.1}$	135.9/139	10.4
0939+3553	$6.47^{+0.08}_{-0.09}$	513^{+163}_{-160}	$1.56^{+0.50}_{-0.49}$	108.6/88	30.8
1034+6001	$6.42^{+0.18}_{-0.06}$	1585^{+897}_{-817}	$0.20^{+0.11}_{-0.10}$	84.3/68	18.2
1034+3939	$6.25^{+0.14}_{-0.18}$	452^{+274}_{-294}	$0.16^{+0.10}_{-0.10}$	145.1/133	7.5
1044+0637	$6.30^{+0.13}_{-0.11}$	419^{+254}_{-248}	$0.75^{+0.45}_{-0.44}$	42.0/40	9.2
1218+4706	$6.38^{+0.19}_{-0.22}$	1656^{+2428}_{-1435}	$0.15^{+0.22}_{-0.13}$	21.8/31	8.1
1238+0927	$6.41^{+0.07}_{-0.07}$	111^{+51}_{-51}	$0.47^{+0.22}_{-0.22}$	313.0/246	13.4
1311+2728	$6.45^{+0.13}_{-0.12}$	527^{+363}_{-363}	$0.36^{+0.25}_{-0.25}$	416.7/434	26.5
1347+1217	$6.42^{+0.07}_{-0.08}$	195^{+148}_{-122}	$0.88^{+0.67}_{-0.55}$	360.7/378	4.0

Note. [a] In the rest frame.

Figure 3. Histograms of column densities of the absorbed power-law spectral fits. The samples and line styles are the same as indicated in Figure 2.

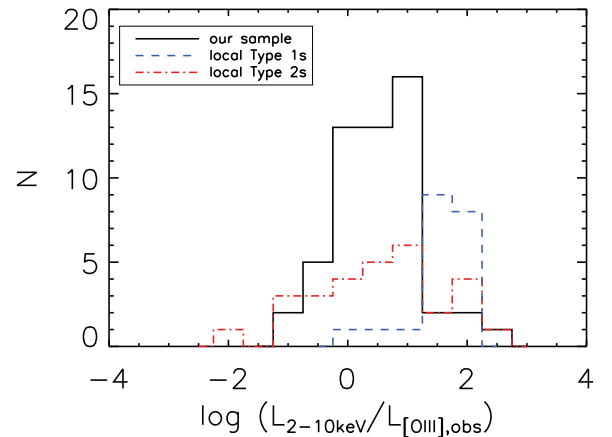(A color version of this figure is available in the online journal.)

Figure 4. Histograms of the ratio of the hard X-ray and observed [O III] λ5007 emission-line luminosity for local Type 1 (dashed blue line) and Type 2 (dash-dotted red line) objects in the samples of Heckman et al. (2005) and our type 2 quasar sample (solid black line).

(A color version of this figure is available in the online journal.)

not affect the statistical result of the photon index distribution. The mean value of our sample is consistent with the result from a sample of type 2 AGNs in the *SWIFT*-BAT survey, which finds a mean value of photon index of the continuum power-law in the energy regime 15–195 keV of $\Gamma = 1.90 \pm 0.27$ (Burlon et al. 2011). It is also roughly consistent with that found in a sample of obscured AGNs selected by *INTEGRAL*, $\Gamma = 1.68 \pm 0.30$. (de Rosa et al. 2012). However, if we use only the results in Table 2 for double-absorber power-law fits, it becomes larger, i.e., $\Gamma = 2.14 \pm 0.60$. This distribution is much like the one found in the best fits of a sample of local Seyfert 2s studied by LaMassa et al. (2009), where more than half of the objects have double-absorbed power laws as their best-fitting model. Since the soft X-ray with steep slope could be biasing the spectral fit with power-law slopes tied, i.e., the slope of AGNs only is flatter than the slope of AGNs plus star formation, this might result in the larger index of double-absorber power law. We show the comparison between our best-fitting results and their samples in Figure 2, where we use different bins for the sample of Burlon et al. (2011) for display purposes.

By excluding those with upper limits or fixed $N_{\rm H,G}$ column densities in the spectral fits, we find that the mean $N_{\rm H}$ of our sample is log $N_{\rm H} = 22.9 \pm 0.9$ cm^{-2} using $N_{\rm H,1}$ for a single

power-law fit and $N_{\rm H,2}$ for a double power-law fit from the best-fitting models listed in Table 2. The $N_{\rm H}$ distribution is consistent with those Seyfert 2s, as shown in Figure 3. We discuss the possible luminosity dependence of obscuration in the following sections.

4.2. The $L_X/L_{\rm [O\,III]}$ Ratio as an Indicator of Obscuration

As the [O III] λ5007 line emission originates in the narrow line region and so is not affected by the circumnuclear obscuration, the ratio between the observed hard X-ray (2–10 keV) and [O III] line luminosity could be used as an indicator of the obscuration of the hard X-ray emission (Mulchaey et al. 1994; Heckman et al. 2005; Panessa et al. 2006; Lamastra et al. 2009, hereafter L09; LaMassa et al. 2009; Trouille & Barger 2010). In Figure 4, we plot a histogram of the $L_X/L_{\rm [O\,III]}$ ratios for our sample listed in Table 2. We also show the observed distributions for type 1 (dashed blue line) and type 2 (dot-dashed red line) AGNs (Heckman et al. 2005). The X-ray to [O III] luminosity ratio of our sample agrees well with that of type 2 AGNs from Heckman et al. (2005) with a Kolmogorov-Smirnov test $P = 0.645$, indicating that this sample is also likely experiencing obscuration. However, the fitted obscuring column densities inferred from the single absorber power-law
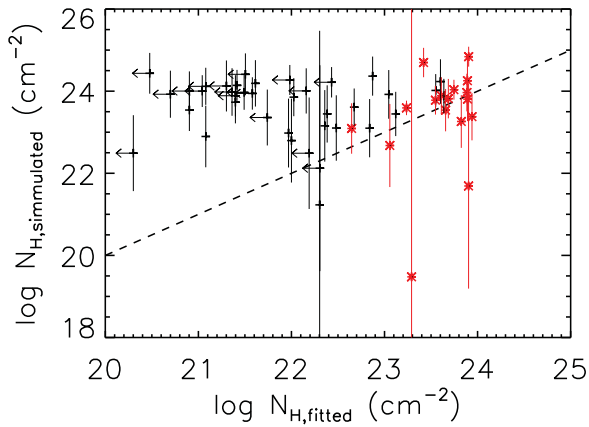
Figure 5. Simulated column densities vs. the values from the best-fitting spectral fits. The dashed line indicates where the two values are equal. The black and red symbols represent the single- and double-absorber model results, respectively.

(A color version of this figure is available in the online journal.)

spectral fits are often too low to be consistent with the $L_X/L_{[O\,III]}$ ratios of type 2 quasars, i.e., the single-absorber model likely underestimates the amount of X-ray obscuration in our sample. Thus, we estimate their obscuration in the following subsection using the X-ray to [O III] ratios.

4.3. Estimation of the Absorbing Column Density

Compared with the local Type 1 AGNs, the derived observed $L_X/L_{[O\,III]}$ ratio in Table 2 implies that the targets in our sample are more highly obscured than would be implied by the fitted column densities N_H from our spectral models, i.e., the column density is underestimated in our spectral fits for at least half of the whole sample. We therefore use the correlation between the hard X-ray and [O III] luminosity for both type 1 and 2 AGNs (Heckman et al. 2005) to more realistically estimate the absorbing column densities of our targets (LaMassa et al. 2009). We employ a Monte Carlo approach to take the dispersion in the Seyfert 1 $L_X/L_{[O\,III]}$ distribution into account. First, we generate 1000 random numbers that follow a Gaussian distribution with the same mean and dispersion as the $L_{2-10\,\mathrm{keV}}/L_{[O\,III]}$ distribution of unobscured (type 1) AGNs in Heckman et al. (2005). For each AGN in our sample, the simulated unabsorbed 2–10 keV X-ray luminosities are computed by multiplying the observed [O III] luminosity by the random draws from the Seyfert 1 $L_{2-10\,\mathrm{keV}}/L_{[O\,III]}$ distribution. The difference between these simulated unabsorbed X-ray luminosities and the observed value is considered to be due to absorption. In order to assess how much absorption is consistent with the difference between the simulated and observed X-ray luminosities, we tabulated the expected fluxes and count rates for a partial covering model with a covering fraction of 0.99 and a photon index fixed at 1.7 and column densities varying from 0 to 10^{25} cm^{-2}. We then interpolated the effective column density $N_{H,sim}$ that predicts a model count rate consistent with the observed count rate for each AGN.

We compare the results from these simulations and the absorbed power-law spectral fits in Figure 5. The fitted N_H values from the single-absorber model (black plus symbols) are systematically lower than the simulated column densities, while the $N_{H,2}$ values from the double-absorber model (red asterisks) are more consistent with the simulated column densities, showing that, not surprisingly, more complex spectral models do a better

Table 5
N_H from Simulation and Spectral Fitting Using the *plcabs* Model
(cm^{-2}, on a Logarithmic Scale)

Source ID	$N_{H,sim}$ (*deviation*)	$N_{H,plcabs}$	ID	$N_{H,sim}$ (*deviation*)	$N_{H,plcabs}$
0011+0056	24.22 (0.37)	22.07	1039+6430	24.41 (0.51)	20.00
0028−0014	23.31 (0.60)		1044+0637	23.38 (0.36)	23.95
0050−0039	24.02 (0.40)	23.61	1106+0357	24.13 (0.62)	21.43
0056+0032	24.27 (0.37)	23.80	1119+6004	22.49 (0.60)	20.00
0120−0055	23.93 (0.44)		1131+3106	24.01 (0.55)	23.00
0123+0044	23.10 (0.71)	22.90	1145+0241	23.93 (0.57)	23.41
0134+0014	24.71 (0.32)		1151+0049	23.85 (0.28)	
0149−0048	>23.79		1153+0326	23.54 (0.34)	21.93
0157−0053	23.82 (0.32)	21.82	1157+6003	24.54 (0.40)	
0210−1001	23.10 (0.80)	22.17	1218+4706	24.84 (0.24)	20.00
0304+0007	23.88 (0.29)	23.61	1226+0131	23.44 (0.42)	22.49
0319−0058	24.27 (0.35)		1227+1248	23.97 (0.46)	23.94
0737+4021	24.40 (0.41)		1228+0050	23.45 (0.54)	23.13
0758+3923	23.89 (0.50)	22.37	1232+0206	24.37 (0.48)	22.92
0801+4412	23.89 (0.30)	23.25	1238+0927	23.54 (0.52)	23.66
0812+4019	22.98 (0.84)	22.07	1243+1220	24.19 (0.56)	<22.52
0815−4304	>22.95		1243−0232	24.11 (0.62)	23.21
0834+5534	22.90 (0.75)	21.04	1301−0058	23.92 (0.59)	23.07
0839+3843	21.23 (1.03)	22.37	1311+2728	24.00 (0.54)	20.00
0840+3838	23.94 (0.39)	20.48	1324+0537	24.12 (0.45)	21.81
0842+3625	24.73 (0.34)		1329+1140	23.73 (0.34)	21.11
0853+1753	24.04 (0.55)	23.01	1337−0128	22.12 (1.51)	21.72
0855+3709	23.61 (0.45)	22.70	1347+1217	23.09 (0.38)	22.50
0900+2053	21.69 (0.83)	21.11	1411+5212	19.48 (1.49)	22.94
0913+4056	23.81 (0.33)	23.56	1430−0056	23.98 (0.58)	22.39
0920+4531	23.97 (0.42)	21.15	1431+3251	24.23 (0.53)	
0921+5153	>23.41		1446+0113	23.67 (0.30)	
0923+0101	24.00 (0.48)	22.89	1449+4221	23.59 (0.35)	23.26
0924+3028	23.78 (0.31)	22.52	1507+0029	23.26 (0.64)	23.01
0939+3553	22.68 (0.52)	22.55	1517+0331	20.90 (1.40)	
0945+0355	23.36 (0.41)	22.57	1606+2725	24.18 (0.41)	
1003+5541	22.49 (0.61)	21.58	1641+3858	23.16 (0.56)	22.29
1022+1929	23.85 (0.32)	22.12	1713+5729	24.43 (0.51)	21.52
1027+0032	24.04 (0.49)		2358−0009	24.14 (0.45)	22.48
1034+6001	24.70 (0.36)	24.78	2358−0022	24.46 (0.43)	
1034+3939	24.25 (0.58)	24.03			

Note. We did not fit the sources reported in Table 3 using the *plcabs* model due to limited photon counts.

job of recovering the intrinsic column density implied by the attenuated X-ray flux relative to the [O III] emission.

Additionally, we used the *plcabs* model in XSPEC (Yaqoob 1997) to fit the spectra in order to approximately take Compton scattering into account. This model assumes a spherical covering that is not likely to be the case but is nevertheless an improvement over fitting with absorption models that do not include scattering. In future work, we will consider more advanced absorption models such as MyTorus for sources with high enough signal to noise to warrant more advanced fitting. The results from fitting with both the simple partial covering model and *plcabs* are shown in Table 5, where the lower limits for the simulated N_H are derived for non-detections based on the upper limits for the photon count rates in Table 3. As shown in Table 5, about half of the sources have a fitted column density $N_{H,plcabs}$ much lower than the simulated $N_{H,sim}$. This indicates that direct spectral fitting still underpredicts the column density even by introducing Compton scattering in some cases, which reaffirms the necessity of using the $L_X/L_{[O\,III]}$ ratio as an indicator of intrinsic obscuration. In summary, these results imply that high signal-to-noise broadband spectra fitted with more

Table 6
Properties of Stacked Fe Kα Emission Lines

	Source ID	$L_X/L_{[O\,III]}$	Net Counts	E_{line} (eV)	EW (eV)
$-0.5 < \log L_X/L_{[O\,III]} < 0$	0056+0032	0.59	84.4	$6.43^{+0.04}_{-0.04}$	1180^{+964}_{-638}
	0758+3923	0.44			
	0840+3838	0.71			
	0945+0355	0.96			
	1145+0241	0.71			
	2358−0009	0.45			
$0 < \log L_X/L_{[O\,III]} < 0.5$	0011+0056	1.7	255.2	$6.45^{+0.30}_{-0.33}$	< 992
	0157−0053	2.2			
	0853+1753	2.5			
	0923+0101	1.1			
	1022+1929	2.1			
	1324+0537	1.7			
	1329+1140	1.5			
$0.5 < \log L_X/L_{[O\,III]} < 1.0$	0050−0039	4.2	586.1	$6.38^{+0.06}_{-0.06}$	360^{+203}_{-166}
	0210−1001	6.3			
	0801+4412	5.5			
	0855+3709	8.6			
	1003+5541	6.0			
	1153+0326	7.7			
	1301−0058	3.5			
	1507+0029	6.3			
$1.0 < \log L_X/L_{[O\,III]} < 1.5$	0812+4018	16.4	1740.4	$6.40^{+0.05}_{-0.06}$	148^{+104}_{-73}
	0924+3028	11.6			
	1119+6004	13.3			
	1226+0131	13.4			
	1347+1217	17.1			
	1641+3858	12.6			

Note. Net counts of the stacked spectra are in the 3–8 keV band; E_{line} and EW are in the rest frame.

complex (and realistic) models are more likely to recover the true (higher) column densities than simple power-law fits. This is also seen in lower luminosity Seyfert 2 galaxies (LaMassa et al. 2009; Rigby et al. 2009; Melendez et al. 2009).

4.4. Iron Line Emission

By visual examination of the spectra, the iron emission line is found in 11 of the type 2 quasars. The line energy and EW, both in the rest frame, are listed in Table 4, as well as the line luminosity, χ^2, and the degrees of freedom in the spectral fitting. For the rest of the sample that does not show a significant Fe Kα component in an individual spectrum, we grouped them according to their observed $L_X/L_{[O\,III]}$ ratio and then applied a "spectral" stacking procedure, also referred to as simultaneous spectral fitting. In Table 6, we show the four bins of the X-ray to [O III] luminosity ratio that are used to group the sources and we exclude those sources with photon counts fewer than 10 in the 2–10 keV band. We load the spectra of the objects in the same bin into XSPEC and only fit their spectra in the 3–8 keV range to minimize the impact of the spectral complexity discussed above. We assume that they have approximately the same properties for the power-law continuum and the iron emission line. The intrinsic line width (σ) in the Gaussian component is fixed at 0.01 keV (i.e., unresolved for CCD spectra) and the photon indices of the continuum power law are fixed at 1.7. The spectrum of each object is not physically shifted to account for redshift since the redshift is instead taken into account in the spectral model. In each group, the normalization of the power-law component and the parameters of the Gaussian component

for each source are tied together between the fits. As we assume that the sources in the same group suffer similar obscuration, tying the parameters can ensure that the sources with similar $L_X/L_{[O\,III]}$ ratios have the same iron line EW. However, the relative intensity (both continuum and emission line) for each source is allowed to be free, which is controlled by a constant factor during fitting. The line energy and EW of the iron line of each bin are shown in Table 6.

We show the correlation between the (effective average) Fe Kα EW and the ratio of hard X-ray and [O III] luminosities ($L_X/L_{[O\,III]}$) in Figure 6. This includes the stacking procedure along with the 11 quasars with prominent iron lines in Table 4 (black plus symbols with error bars), the four groups classified by their $L_X/L_{[O\,III]}$ ratio in Table 6 (blue plus symbols without error bars), and the sample of type 2 Seyfert galaxies from LaMassa et al. (2009; red asterisks with error bars). Two objects (SDSS J1218+4706 and SDSS J1238+0927) are included in both our sample and the LaMassa et al. (2009) sample; we use the EW and luminosity in Table 4 to make the plots as both papers give similar results. In order to fit the correlation by taking the upper limits into account, we use the survival analysis program ASURV (Rev. 1.2), which implements the method presented in Isobe & Feigelson (1990) and Lavalley et al. (1992) to investigate the correlation between these two parameters (log EW in units of eV and $L_X/L_{[O\,III]}$). ASURV uses the bivariate data algorithm by Isobe et al. (1986). The correlation coefficient found in the survival analysis is -0.52 ± 0.10 with a $>3\sigma$ significance.

We also investigate the correlation between the iron emission line luminosity and the [O III] luminosity by applying survival
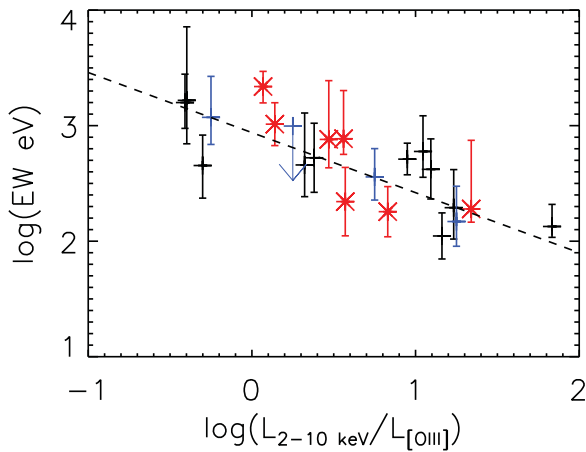
Figure 6. EW of Fe Kα emission line vs. $L_{2-10\,\mathrm{keV}}/L_{\mathrm{[O\,III]}}$. The data in black and blue are from Tables 4 and 6 in our sample and those in red are from LaMassa et al. (2009).

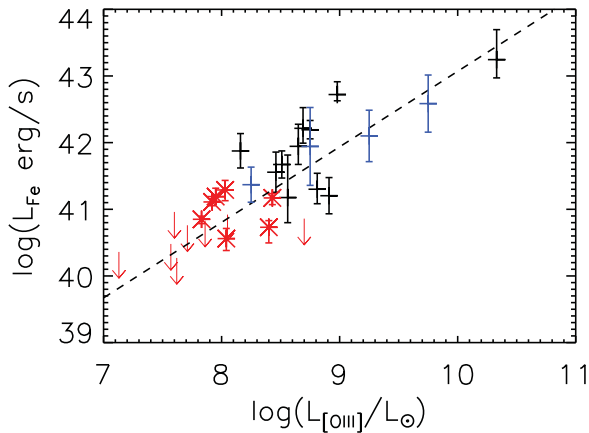(A color version of this figure is available in the online journal.)

Figure 7. Fe Kα luminosity vs. [O III] luminosity. The data in red are the sample of type 2 Seyfert galaxies from LaMassa et al. (2009). The black symbols indicate the quasars having iron line detections listed in Table 4 and the blue symbols indicate those from stacking.

(A color version of this figure is available in the online journal.)

analysis. This is shown in Figure 7, which includes the 11 individual objects listed in Table 4 (symbols in black), the sample from LaMassa et al. (2009; symbols in red), and those in our sample with no visually detected iron lines (symbols in blue). For those not listed in Table 4, we grouped them in bins defined by their [O III] luminosities. The iron line luminosity in each bin is calculated as the mean of $L_{\mathrm{[O\,III]}}$ by multiplying by the ratio of $\langle f_{\mathrm{Fe}}\rangle/\langle f_{\mathrm{[O\,III]}}\rangle$, where $\langle f_{\mathrm{Fe}}\rangle$ and $\langle f_{\mathrm{[O\,III]}}\rangle$ are the means of the iron line and [O III] fluxes in each bin, respectively. The mean values of the iron line luminosity in the $L_{\mathrm{[O\,III]}}$ bins are listed in Table 7, where the error of L_{Fe} is calculated using error propagation of δf_{Fe} and $\delta f_{\mathrm{[O\,III]}}$. The slope of the linear regression fit is 1.13 ± 0.15, with the significance of correlation greater than 99.99%. Compared with the value of 1 with a scatter of 0.5 dex given by Ptak et al. (2003) and 0.7 ± 0.3 by LaMassa et al. (2009), it implies that the Fe Kα line luminosity is roughly tracking the intrinsic AGN luminosity in a similar fashion as lower luminosity obscured AGNs.

4.5. Luminosity Dependence of Obscuration

LaMassa et al. (2011) studied a sample of 45 type 2 Seyfert galaxies selected based on their mid-IR continuum and [O III] $\lambda 5007$ and emission line fluxes. They found that the
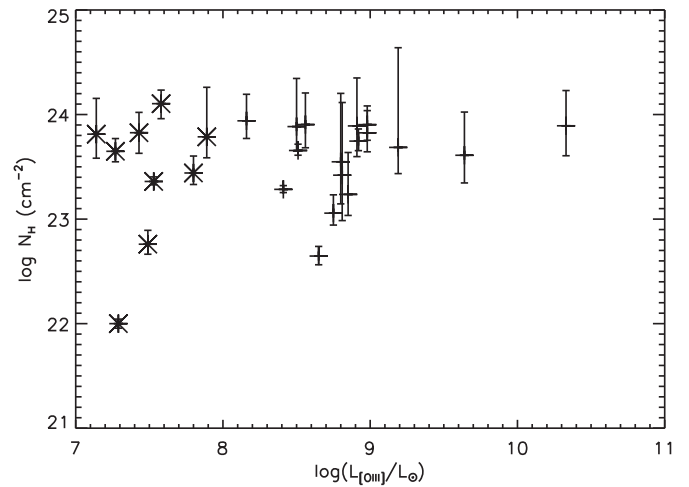
Figure 8. Column density of the second absorber ($N_{\mathrm{H},2}$) in Table 2 vs. [O III] luminosity. The crosses are our type 2 quasar sample, while the asterisks are the type 2 Seyferts from LaMassa et al. (2009). There is no correlation between column density and luminosity.

Table 7
The Means of [O III] and X-Ray Luminosities and Their Ratios in $L_{\mathrm{[O\,III]}}$ Bins

$\log L_{\mathrm{O\,III}}$ Range ($L_\odot$)	$\langle \log L_{\mathrm{O\,III}}\rangle$ ($L_\odot$)	$\langle L_{\mathrm{X}}\rangle$ (10^{44} erg s^{-1})	$\langle L_{\mathrm{X}}/L_{\mathrm{O\,III}}\rangle$	$\langle L_{\mathrm{Fe}}\rangle$ (10^{42} erg s^{-1})
8.0–8.5	8.35 ± 0.14	0.04 ± 0.01	6.01 ± 2.80	0.23 ± 0.06
8.5–9.0	8.75 ± 0.15	0.30 ± 0.21	13.5 ± 8.17	0.88 ± 0.42
9.0–9.5	9.21 ± 0.13	0.38 ± 0.21	5.73 ± 3.21	1.26 ± 0.40
>9.5	9.88 ± 0.25	2.04 ± 0.66	6.51 ± 0.67	3.85 ± 1.55

observed hard X-ray to [O III] flux ratios are one order of magnitude lower on average than those of type 1 Seyfert galaxies (in agreement with Heckman et al. 2005) and they show a continuum of inferred X-ray obscuration without a clear separation into Compton-thin and Compton-thick populations. Here, we similarly find that there is no strong break in the distributions of either the fitted N_{H} distribution or the $L_{\mathrm{X}}/L_{\mathrm{[O\,III]}}$ ratio for high-luminosity type 2 AGNs (Figures 3 and 4). We also find that the correlation between the Fe Kα and [O III] luminosities is evidently the same between this sample of type 2 quasars and type 2 Seyfert galaxies. Finally, Figure 6 shows that the correlation between the EW of the iron line and the $L_{\mathrm{X}}/L_{\mathrm{[O\,III]}}$ ratio is also the same for both the low-luminosity (Seyfert) and high-luminosity (quasar) type 2 AGNs. Taken together, these results show that low- and high-luminosity optically selected type 2 AGNs have similar properties with respect to their X-ray obscurations.

We examine the possible luminosity dependence of obscuration more directly in Figure 8, in which we plot the column density of the second absorber versus the observed [O III] luminosity for those AGNs having double-absorber power-law fits in Table 2. We also add the corresponding data for the type 2 Seyferts from LaMassa et al. (2009). There is no tendency for the column density to be correlated with the [O III] luminosity (over a range of more than three orders of magnitude in luminosity). Finally, in Figure 9, we plot the hard X-ray luminosity versus the [O III] luminosity for the combination of our type 2 quasar sample and the LaMassa et al. type 2 Seyfert sample. Using survival analysis to account for the objects with upper limits on the X-ray luminosity, we find a best-fit slope in the log–log plot of 0.88 ± 0.11 (consistent with no significant luminosity-dependent X-ray obscuration), with significance of correlation
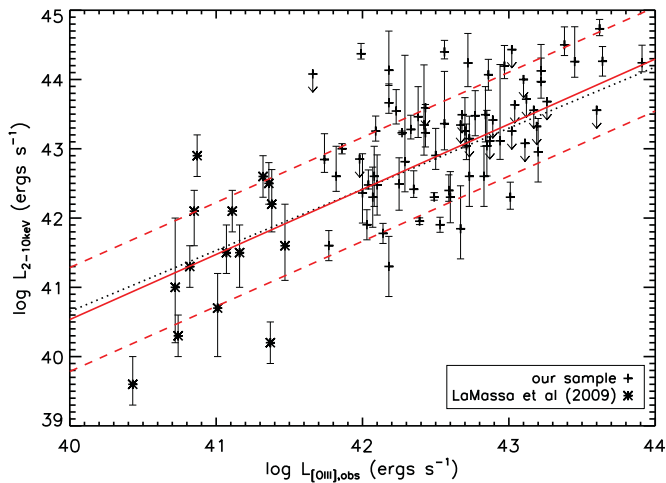
Figure 9. log of the 2–10 keV X-ray luminosity plotted vs. the log of the [O III] luminosity. The pluses show our type 2 quasar sample, while the asterisks are the type 2 Seyfert galaxies in LaMassa et al. (2009). The best fit (dotted line) slope (which includes the non-detections in X-rays) is 0.88 ± 0.11 and is not significantly different from unity. Thus, the degree of X-ray obscuration does not depend on AGN luminosity. The solid red line indicates the best fit slope of the sample of type 1 AGNs given by Jin et al. (2012) with a shift of 1.26 dex downward to line up with the sample in our paper. The dashed red lines indicate the $\pm 1\sigma$ deviation for the data points in this plot.

(A color version of this figure is available in the online journal.)

>99.99%. In fact, type 1 AGNs show a systematic decrease in their ratios of hard X-ray to bolometric luminosity at increasing bolometric luminosity (e.g., Marconi et al. 2004; Vasudevan & Fabian 2007; Vasudevan et al. 2009; Lusso et al. 2010). If the [O III] luminosity is proportional to the bolometric luminosity and if the amount of X-ray obscuration is independent of AGN luminosity, then the relationship in Marconi et al. (2004) would imply a slope of ∼0.8. This is fully consistent with the fitted slope in Figure 9. Recently, Jin et al. (2012) reported a nearly linear correlation between $L_{[O III]}$ and $L_{2-10\,keV}$ of a sample of type 1 AGNs selected from the cross-correlation of the 2XMMi and SDSS DR7 catalogs. We show the correlation with the slope found by them in Figure 9 with the 1σ deviation of our sample, where the line is shifted 1.26 dex downward to line up with the sample in this paper. This offset between the type 1 sample by Jin et al. (2012) and our type 2 sample is consistent with that reported by Heckman et al. (2005), indicating that the $L_X/L_{O III}$ ratio is still a good indicator of intrinsic obscuration for high-luminosity AGNs.

Additionally, we compare the ratio of their X-ray and [O III] luminosity with their geometric means in Figure 10. There appears to be a slight correlation (slope 0.24 ± 0.09 in log–log scale) between the two quantities, as shown in the upper panel of Figure 10. However, if we exclude those highly obscured sources with $L_X/L_{O III} < 1$, this correlation becomes negligible, i.e., the slope is nearly zero (see the lower panel of Figure 10). Comparing both cases, we find that the "correlation" in the top panel of $L_X/L_{O III}$ versus $(L_X L_{O III})^{1/2}$ is driven by the highly-obscured AGNs at lower luminosity.

4.6. The Fraction of Compton-thick AGNs

In order to explain the X-ray background (XRB) spectrum above 10 keV, Gilli et al. (2007) predict that the population of Compton-thick AGNs is as numerous as that of Compton-thin ones in their synthesis model of XRB fitting.

In Figure 11, we plot the $L_X/L_{[O III]}$ ratio versus column densities we derived from the simulations described in Section 4.3.
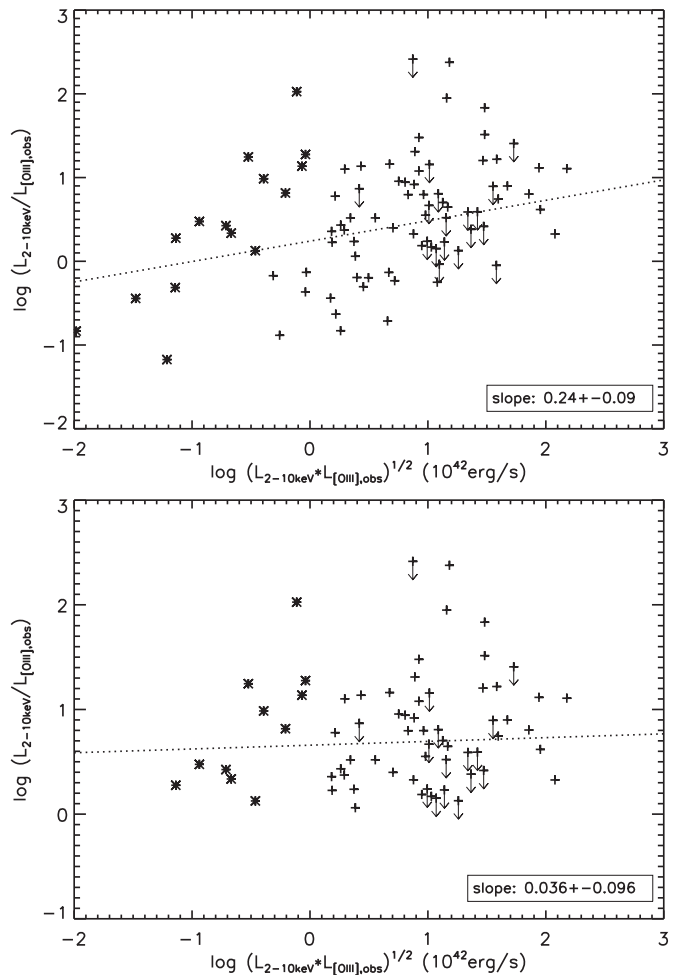

Figure 10. $L_X/L_{[O III]}$ vs. $(L_X \cdot L_{O III})^{1/2}$. The upper panel includes all objects from our sample (plus symbols) and LaMassa et al. (2009, asterisk symbols). The lower panel excludes those with $L_X/L_{O III} < 1$.

Since $N_{H,sim}$ is derived from the difference between the typical Seyfert 1 $L_X/L_{[O III]}$ value and our observed $L_X/L_{[O III]}$, it is not surprising that we find that the $L_X/L_{[O III]}$ ratio decreases as the simulated $N_{H,sim}$ increases. We designate a source as a Compton-thick candidate if the 1σ confidence interval of the simulated column density exceeds 1.6×10^{24} cm^{-2} in Figure 11. In addition, sources with an iron line EW larger than 1 keV in Table 4 are also considered to be Compton thick, although the errors are often large. Also, note that in some cases there is a possibility that an AGN can be Compton thick even though its Fe K emission line has a low EW (e.g., Mkn 231). By also including the three sources that have no hard X-ray photons detected, we find that 39 quasars out of 71 ($55 \pm 9\%$) are classified as Compton thick. We flagged them in Tables 2 and 3. Of course, the Compton-thick fraction calculated in this way has a large uncertainty due to the inaccuracy of the simulated obscuration. Taking the lower error bars of $N_{H,sim}$ into account, there are 30 sources with $N_{H,sim} - \sigma_{N_{H,sim}} > 10^{23.5}$ cm^{-2}, which is still a significant fraction of heavily obscured sources.

This selection is basically equivalent to the approach based on $L_X/L_{O III}$ in V10. LaMassa et al. (2011) found that a majority of Compton-thick AGNs selected based on various obscuration diagnostics have ratios of 2–10 keV flux to intrinsic flux an order of magnitude lower than the mean values for Seyfert 1s. If we adopt the mean $L_X/L_{O III}$ value of type 1 Seyferts found
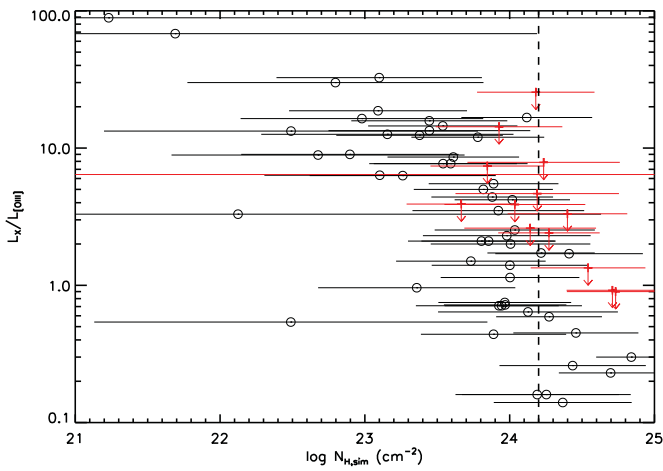
Figure 11. Observed hard X-ray to [O III] luminosity ratio vs. simulated column density. The open circles represent the AGNs whose hard X-ray luminosities were derived from their spectral fits listed in Table 2. The red plus symbols represent upper limit cases in Table 3. The dashed vertical line denotes the region where $N_{H,simulated} > 1.6 \times 10^{24}$ cm^{-2}. These objects are designated as Compton-thick AGNs in this work.

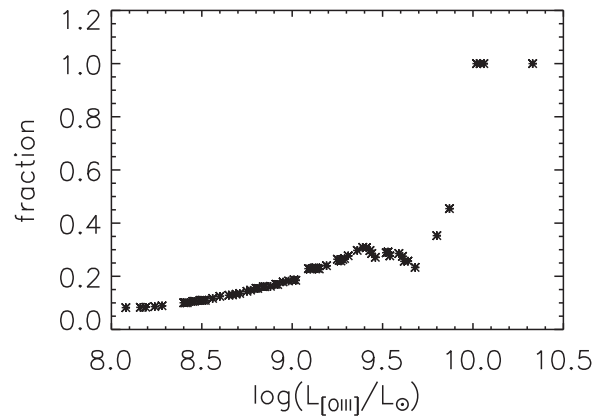(A color version of this figure is available in the online journal.)

Figure 12. Completeness of our sample in the catalog of R08 as a function of [O III] luminosity. The fraction is calculated as the number of AGNs in our sample above a given [O III] luminosity (X-axis) divided by the number of all the AGNs in the R08 sample above the same [O III] luminosity.

in Heckman et al. (2005), we find that the sources marked as Compton thick in Table 2 agree with the conclusion of flux ratio in LaMassa et al. (2011), except for a few outliers.

4.7. Sample Completeness and Selection Bias

As stated above, in a sample of 25 obscured quasars optically selected from the SDSS, V10 estimated the intrinsic X-ray luminosity from the observed [O III] emission line flux using the results of Mulchaey et al. (1994) and compared it with the observed X-ray luminosities, i.e., similar to our simulation procedure, although our simulations take the dispersion in the Seyfert 1 distribution into account. V10 conclude that a quasar could be identified as Compton thick if the ratio between the observed and predicted X-ray luminosities is less than 0.01 and find the fraction of Compton-thick AGNs to be 65%. However, they point out that the [O III]-based selection results in an Eddington bias that would naively lower the observed $L_X/L_{[O III]}$ ratios and estimate that the true fraction is likely closer to 50% on the basis of the observed L_X/L_{MIR} values for their sample, where L_{MIR} refers to the mid-IR luminosity.

The V10 sample is selected from the catalog of 291 type 2 quasars in Z03 with $L_{[O III]} > 10^{9.28} L_{\odot}$ (note that the [O III] luminosities used by V10 are from Z03, which are slightly different from those given by R08 due to a different [O III] line fitting procedure). This sample had complete X-ray coverage. However, the R08 catalog is significantly larger, with 887 type 2 quasars selected by applying the same criteria to newer and more extensive SDSS data. This increase in sample size, plus the larger range in $L_{[O III]}$ that we have probed, means that our sample is not complete with respect to the optical selection. Also, as discussed in V10, the selection based on [O III] line may miss some type 2 AGNs due to extinction. Thus, it is necessary to discuss how the completeness may affect our estimation of the fraction of Compton-thick AGNs. In Figure 12, we show the completeness of our sample in the catalog of R08, which is the number of AGNs in our sample above a given [O III] luminosity divided by the number of AGNs in the R08 sample above the same [O III] luminosity. Although our sample only covers a small fraction (∼8%) of the parent sample in R08

over most of the [O III] luminosity range, the completeness rises rapidly at higher luminosities, reaching over >20% in the luminosity range studied by V10 ($L_{[O III]} > 10^{9.10} L_{\odot}$ according to the new measurement of [O III] luminosity by R08).

If we limit the [O III] luminosity range of our sample to that in V10, the Compton-thick fraction becomes 56% (19 out of 34) with $L_{[O III]} > 10^{9.10} L_{\odot}$, consistent with the fraction reported in V10. When we adopt an [O III] luminosity above $10^{9.50} L_{\odot}$, the Compton-thick fraction is 53% (8 out of 15).

Although 45 out of the total 72 sources are on-axis targets, only 13 quasars in our sample were initially targeted observations by *Chandra* and *XMM-Newton* and were not obviously selected independently of their X-ray properties. The others are either serendipitous objects in the field of view (27) or were observed in X-rays based on their [O III] luminosities (32). Thus, the majority of our sample were not observed in X-rays based on their known X-ray properties. From this point of view, we can safely claim that our sample is not X-ray biased.

5. SUMMARY

We have presented the hard (2–10 keV) X-ray spectral properties of 71 type 2 quasars in the redshift range of $z \sim 0.05$–0.73 from *Chandra* and *XMM-Newton* archival data that were selected based on their [O III] $\lambda 5007$ emission line luminosity. This is the largest sample of optically selected obscured quasars studied in X-rays to date. Their observed [O III] luminosities range from 10^8–$10^{10.3} L_{\odot}$.

Of these 71 objects, 17 have limited photons detected and we ascribed 3σ upper limits to their X-ray fluxes. For the remainder, we fit their X-ray spectra by assuming a single absorbed power law to probe their spectral slope and circumnuclear obscuration. We use a more complicated model (a double-absorber power law) to re-do the spectral fits on 17 sources. We also fit the Fe Kα fluorescent emission line in individual sources. For the others, we grouped them in four bins according to their observed $L_X/L_{[O III]}$ ratios and $L_{[O III]}$ and jointly fit their spectra to investigate the Fe Kα feature. We also used a more physically realistic model to simulate the X-ray spectrum, which included partial covering by the absorber and the effects of Compton scattering. Our main results are summarized as follows.

1. For the 54 sources fit with an absorbed power law, we find that the average value for the power-law index is $\langle \Gamma \rangle = 1.87 \pm 0.74$. The average column density of our

sample from the direct spectral fit is $\log N_H = 22.9 \pm 0.9 \text{ cm}^{-2}$.

2. The distribution of the $L_X/L_{[O\,III]}$ ratio of our type 2 quasar sample agrees with that of local lower luminosity type 2 Seyferts studied previously, indicating that they are experiencing similar amounts of X-ray obscuration. Based on the small ratios of $L_X/L_{[O\,III]}$, we find that the single-absorber power-law model underestimates the intrinsic X-ray obscuration. The double-absorber power-law model we applied to the 17 brightest sources also gave a higher column density than the single-absorber model.

3. We constructed a more physically realistic model with partial covering of the central source and Compton scattering to simulate the intrinsic column densities that produced the observed low $L_X/L_{[O\,III]}$ ratio. We find that about half of our sample have simulated column densities one order of magnitude higher than from their single power-law spectral fits, but with a significantly better agreement with the double power-law model results.

4. We investigated the Fe Kα features directly detected in 11 individual sources and the rest in groups by stacking (jointly fitting) their spectra. The anti-correlation between the iron line EW and the $L_X/L_{[O\,III]}$ ratio confirms the relationship studied previously (Krolik & Kallman 1987; Bassani et al. 1999; LaMassa et al. 2009). Also, we find that the iron line luminosity correlates well with the [O III] line luminosity, extending the relation seen in type 2 Seyferts to higher luminosities. These correlations illustrate that the weak observed hard X-ray emission is due to the heavy absorption around the central SMBH, not due to intrinsically weak X-ray emission. The consistency of these correlations with those found in low-luminosity Seyfert galaxies supports the standard model of AGN at the high-luminosity end.

5. By combining our analysis with results for type 2 Seyferts from LaMassa et al. (2009, 2011), we find no dependence of the simulated absorbing column densities on AGN luminosity. We also find a nearly linear relationship between the [O III] and X-ray luminosities. These results show that the amount of X-ray obscuration does not depend significantly on AGN luminosity (over a range in luminosity of over three orders of magnitude).

6. Based on the observed $L_X/L_{[O\,III]}$ ratio and the simulated column densities, we find that about half of the total 71 quasars would be classified as Compton-thick AGNs. When limiting the $L_{[O\,III]}$ range to higher values, the Compton-thick fraction does not change significantly. However, more accurate quantification of the Compton-thick fraction and its dependence on intrinsic luminosity requires a larger sample.

APPENDIX A

OBJECTS STUDIED IN THE LITERATURE

35 quasars in our sample were also found in papers of X-ray studies of Type 2 AGNs (Vignali et al. 2004, hereafter V04, V06, V10, LM09, P06, and L09); these objects are flagged in the last column of Table 1. There are 17 objects studied in V04, but only SDSS J1226+0131 has *XMM* data and others are observed by *ROSAT*. Two objects (SDSS J0115+0015 and

SDSS J0243+0006) in P06 were included in Z03, but the [O III] luminosity cut excludes them in R08. Therefore, we remove these two objects in this paper.

Objects with limited photon counts. SDSS J0120−0050, SDSS J0134+0014, SDSS J0319−0058, SDSS J0737+4021, SDSS J1027+0032, SDSS J1446+0113, SDSS J1517+0331, and SDSS J2358−0022 have their X-ray luminosity given as a 3σ upper limit in our work (see Table 3). However, the de-absorbed X-ray luminosities of these sources in V06 and V10 are not listed as upper limits. The luminosities are based on directly converting from their observed 2–8 keV count rates and are about one order of magnitude lower than our upper limits.

SDSS J0149−0048, SDSS J0815+4304, SDSS J0842+3625, SDSS J0921+4531, and SDSS J1157+6003 have upper limits on the observed flux and derived X-ray luminosity given in our work, V06, and V10. However, we find that our values are systematically one order of magnitude larger than those in V04, V06, and V10. This difference is due to our assumption of an intrinsic column density of 10^{23} cm^{-2} in converting the source count rates to flux, while only Galactic absorption was assumed by V04, V06, and V10.

SDSS J0050-0039. The spectral parameters given by V06 are $N_H = 3.75 \times 10^{23} \text{ cm}^{-2}$ and $\Gamma = 1.78$ and the derived de-absorbed 2–10 keV luminosity is $7.2 \times 10^{44} \text{ erg s}^{-1}$. These values are consistent with our analysis of the same *Chandra* observation (Obs ID: 5694) and we also derive the observed 2–10 keV luminosity of $1.8 \times 10^{44} \text{ erg s}^{-1}$.

SDSS J0123+0044. This object has enough photons to constrain the spectral parameters. Leaving the photon index as a free parameter in V10's initial spectral fitting resulted in a very flat spectrum. V10 then fixed it at 2 and derived a column density of $N_H = 1.44 \times 10^{23} \text{ cm}^{-2}$, which is twice our value. However, we did not fix the photon index and obtained a value of $\Gamma = 0.69$.

SDSS J0157+0053. The *Chandra* observation (Obs ID:7750) is studied by both V10 and us. The de-absorbed X-ray luminosity of this *Chandra* observation from our work is one order of magnitude larger than that given by V10. However, we also found an *XMM* observation available, which has many more photon counts than the *Chandra* data, to constrain the spectral parameters. The result of multiple observations is shown in Appendix B.

SDSS J0210-1001. P06 presented the spectral properties of this object by analyzing the *XMM* observation (Obs ID: 0204340201), which gives a column density of $N_H = 2.3 \times 10^{22} \text{ cm}^{-2}$ and a flat photon index of $\Gamma = 0.46$. V06 re-analyzed the data but only gave the de-absorbed 2–10 keV luminosity, which is close to the value from P06. We have similar results in this paper.

SDSS J0801+4412. We obtain similar spectral parameters and flux for this object as P06 did. The column density given by V06 is $N_H = 4.29 \times 10^{23} \text{ cm}^{-2}$, while it is $4.08 \times 10^{23} \text{ cm}^{-2}$ in our work.

SDSS J0812+4018. The best-fit photon index and absorption of SDSS J0812+4018 in V10 are $\Gamma = 2.6$ and $N_H = 2.14 \times 10^{22} \text{ cm}^{-2}$. Our results are $\Gamma = 1.91$ and $N_H = 9.3 \times 10^{21} \text{ cm}^{-2}$, a flatter spectral slope and a slightly smaller obscuration.

SDSS J0920+4531. Neither we nor V10 were able to constrain the column density from the spectral fit. V10 fixed the photon index at $\Gamma = 2$ and our value is $\Gamma = 1.38$; our value of the derived X-ray luminosity is twice as large as theirs.

SDSS J1039+6430. Very limited photons are detected; the spectral fit used by both V10 and us fixed the photon index. V10 also fixed the column density at the Galactic value, while we

derived an upper limit for it. Our results are similar to the values in V10.

SDSS J1153+0326. V06 fit the spectrum first with a power law and Galactic absorption only and they got a flat photon index of $\Gamma = 0.56$. This is consistent with our result in Table 2. They then fixed the index at $\Gamma = 2$ and got an absorption of $N_H = 1.54 \times 10^{22}$ cm^{-2}.

SDSS J1218+4706. Our spectral fit results are very similar to those from L09. Both works used a double-absorber power-law model in the spectral fitting.

SDSS J1226+0131. The *XMM* observation (Obs ID: 0110990201) is studied by both V04 and P06. The best-fitting spectrum of SDSS J1226+0131 in V04 gives a flat photon index of $\Gamma = 1.3$ and column density $N_H = 1.26 \times 10^{22}$ cm^{-2}. In P06, the simple power-law model fitting gives $\Gamma = 1.41$ and $N_H = 2.0 \times 10^{22}$ cm^{-2}. Our N_H value are close to their results. The observed hard X-ray luminosity is consistent with the two papers.

SDSS J1228+0050. The column density from the spectral fit by V10 is $N_H = 1.52 \times 10^{23}$ cm^{-2}, which is very close to our value of $N_H = 1.32 \times 10^{23}$ cm^{-2}. The photon index given by both works is slightly different: $\Gamma = 1.9$ in their paper and 1.55 in ours, but they are consistent if the uncertainty is considered.

SDSS J1232+0206. P06 fixed both the photon index and the column density ($\Gamma = 1.7$ and $N_H = 1.0 \times 10^{23}$ cm^{-2}) in the spectral fitting. We got $\Gamma = 2.11$ and $N_H = 7.45 \times 10^{22}$ cm^{-2}. Our derived flux value is consistent with the results of P06 to within a factor of two.

SDSS J1238+0927. Our spectral fit results are very similar to those from L09. Both works used a double-absorber power-law model in the spectral fitting.

SDSS J1641+3858. The spectral properties obtained by P06 are very close to the values in our paper. V06 got a column density slightly higher but still consistent with our value.

SDSS J2358-0009. This object was considered to be a serendipitous source with a large off-axis angle in the *Chandra* observation (Obs ID: 5699). Only flux and luminosity upper limits were given in V06 due to the very limited photon counts. This dataset is ruled out for this object by the search radius described in Section 2. Instead, we found that it is covered by two *XMM* observations (see Table 1). We performed a moderate-quality spectral fit using the *XMM* data.

APPENDIX B

OBJECTS WITH MULTIPLE OBSERVATIONS

SDSS J0056+0032. This object was observed by *XMM* (Obs ID: 0303110401) and *Chandra* (Obs ID: 7746) in 2005 and 2008, respectively. The *XMM* observation had 59 total photons detected, which allows us to perform a moderate-quality spectral fit. The *Chandra* observation detected only 6 photons, which is not sufficient for a spectral fit. Thus, we do not report the spectral results of the *Chandra* observation in Table 2 and adopt the photon index, column density, and observed X-ray luminosity from the *XMM* data in the discussion.

SDSS J0157-0053. The *Chandra* observation (Obs ID: 7750) has 23 photons detected, which allows a moderate quality spectral fit. The photon index is $\Gamma = -0.47$ for this *Chandra* observation in the single-absorber power-law model and results in a large data-to-model ratio. Thus, the double-absorber power-law model is used in the spectral fit instead. The *XMM* observation (Obs ID: 0303110101) detected ∼500 photons and the spectral fit gives $\Gamma = 1.64$. Due to the insufficient

photon counts in the *Chandra* observation, we use the spectral properties and derived flux from the *XMM* observation in the sample statistics.

SDSS J0758+3923. There are two *XMM* observations available for this object, Obs ID: 0406740101 and Obs ID: 0305990101. No significant flux variability is observed. The spectral fit parameters for both individual and combined observations are listed in Table 2. We use the luminosity information from the observation with longer exposure time. The spectral plot of *XMM*-0406740101 is shown in Figure 1 and Figure 13 shows the simultaneous spectral fit for multi-observations.

SDSS J0834+5534. Also known as 4C 55.16. Two *Chandra* observations (Obs ID: 1645 and Obs ID: 4940) and one *XMM* observation (Obs ID: 0143653901) are found to cover 0834+5534. The *XMM* imaging shows a point-like morphology of this object, but it is extended in the *Chandra* observations. The extraction circle radii on the *Chandra* and *XMM* images are 2$\farcs$5 and 38$''$, respectively. The 2–10 keV flux measured from the *XMM* data is one order of magnitude higher than that from the *Chandra* observations (see Table 2). Since it is radio loud, the extended emission is probably due to the jets. Therefore, we use the results of the 2$\farcs$5 extraction region in the *Chandra* data. A simultaneous spectral fit of both *Chandra* observations is shown in Figure 13.

SDSS J0900+2053. Two *Chandra* observations (Obs ID: 10463 and Obs ID: 7897) and one *XMM* observation (Obs ID: 0402250701) are found to cover 0900+2053. The *Chandra* observations show an extended morphology in X-ray emission. The star formation rate of the galaxy is 12.5 $M_\odot$ yr^{-1} given by the MPA/JHU DR7 of SDSS.[6] We extracted the spectra from concentric regions with radii of 2$\farcs$5, 10$''$, and 20$''$. The soft X-ray fluxes of the two larger regions are 7 and 10 times that of the 2$\farcs$5 region, while the hard X-ray fluxes of the two larger regions are only 2 and 3 times that of the smallest region. Thus, the extended emission is dominated by soft X-ray photons from star formation. We use the 2$\farcs$5 region to estimate the quasar emission in this paper. The simultaneous spectral fit of both *Chandra* observations is shown in Figure 13.

SDSS J0913+4056. This is a hyperluminous IR galaxy. Two *Chandra* observations (Obs ID: 10445 and Obs ID: 509) and one *XMM* observation (Obs ID: 0147671001) are found to cover SDSS J0913+4056. Like SDSS J0900+2053, soft X-ray photons dominate the extended emission and we use a 2$\farcs$5 region for the spectral analysis of the quasar emission. A simultaneous spectral fit of both *Chandra* observations is shown in Figure 13. The spectral parameters from our fits are consistent with the original papers that studied these three observations (Iwasawa et al. 2001; Piconcelli et al. 2007; Vignali et al. 2011). However, they came to different conclusions whether it was Compton thin or Compton thick.

SDSS J1227+1248. Three *Chandra* observations (Obs ID: 5912, Obs ID: 9509, and Obs ID: 9510) and one *XMM* observation (Obs ID: 0210270101) have SDSS J1227+1248 covered in the field of view. The simultaneous fit of the three *Chandra* datasets is shown in Figure 13. However, we only use the *XMM* observation in the double power-law spectral fit to derive the spectral properties.

SDSS J1311+2728. This object was observed by *XMM* (Obs ID: 0021740201) and *Chandra* (Obs ID: 12735) with exposure times of 44 ks and 8 ks, respectively. The *XMM* observation has 588 total X-ray photons detected, while only
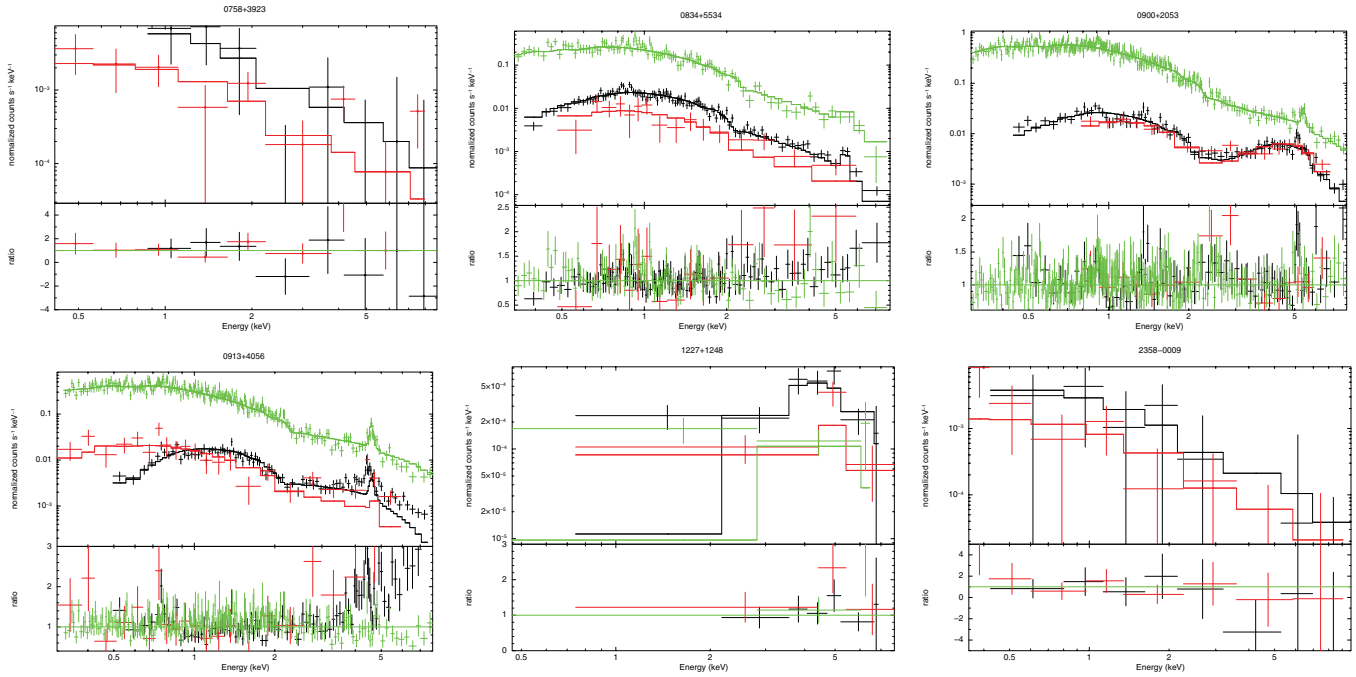
---

[6] http://www.mpa-garching.mpg.de/SDSS/DR7/

Figure 13. *SDSS J0758+3923*: the symbols in black indicate the data obtained by *XMM*-0305990101 and the red symbols are from *XMM*-0406740101. Only PN detections are shown in this plot; *SDSS J0834+5534*: the symbols in black indicate the data obtained by *Chandra*-4940, the red symbols are from *Chandra*-1645, and the green symbols are PN data of *XMM*-0143653901; *SDSS J0900+2053*: the symbols in black indicate the data obtained by *Chandra*-10463, the red symbols are from *Chandra*-7897, and the PN data of *XMM*-0402250701 are shown in green; *SDSS J0913+4056*: the symbols in black and red indicate the data obtained by *Chandra*-10445 and *Chandra*-509, respectively, and the symbols in green indicate the PN data from *XMM*-0147671001; *SDSS J1227+1248*: the symbols in black, red, and green indicate the data obtained by *Chandra*-5912, 9509, and 9510, respectively; *SDSS J2358-0009*: the symbols in black and red indicate the data obtained by *XMM*-0303110301 and 0303110801, respectively.

(A color version of this figure is available in the online journal.)

19 photons are captured by *Chandra*. Therefore, the spectral properties of SDSS J1311+2728 presented in this paper are from the *XMM* observation.

SDSS J2358-0009. This object is observed by two *XMM* observations (Obs ID: 0303110301 and Obs ID: 0303110801). The simultaneous fit of both observations is shown in Figure 13.

REFERENCES

Akylas, A., Georgantopoulos, I., Georgakakis, A., Kitsionas, S., & Hatziminaoglou, E. 2006, A&A, 459, 693
Allen, C., Jerius, D. H., & Gaetz, T. J. 2004, Proc. SPIE, 5165, 423
Antonucci, R. 1993, ARA&A, 31, 473
Avni, Y. 1976, ApJ, 210, 642
Barger, A. J., Cowie, L. L., Mushotzky, R. F., et al. 2005, AJ, 129, 578
Bassani, L., Dadina, M., Maiolino, R., et al. 1999, ApJS, 121, 473
Becker, R. H., White, R. L., & Helfand, D. J. 1995, ApJ, 450, 559
Brinchmann, J., Charlot, S., White, S. D. M., et al. 2004, MNRAS, 351, 1151
Burlon, D., Ajello, M., Greiner, J., et al. 2011, ApJ, 728, 58
Cash, W. 1979, ApJ, 228, 939
Condon, J. J., Cotton, W. D., Greisen, E. W., et al. 1998, AJ, 115, 1693
de Rosa, A., Panessa, F., Bassani, L., et al. 2012, MNRAS, 420, 2087
Dickey, J. M., & Lockman, F. J. 1990, ARA&A, 28, 215
Dwelly, T., & Page, M. J. 2006, MNRAS, 372, 1755
Fiore, F., Grazian, A., Santini, P., et al. 2008, ApJ, 672, 94
Gilli, R., Comastri, A., & Hasinger, G. 2007, A&A, 463, 79
Gilli, R., Vignali, C., Mignoli, M., et al. 2010, A&A, 519, A92
Hao, L., Strauss, M. A., Fan, X., et al. 2005, AJ, 129, 1795
Heckman, T. M., Kauffmann, G., Brinchmann, J., et al. 2004, ApJ, 613, 109
Heckman, T. M., Ptak, A., Hornschemeier, A., & Kauffmann, G. 2005, ApJ, 634, 161
Isobe, T., & Feigelson, E. D. 1990, BAAS, 22, 917
Isobe, T., Feigelson, E. D., & Nelson, P. I. 1986, ApJ, 306, 490
Iwasawa, K., Fabian, A. C., & Ettori, S. 2001, MNRAS, 321, L15
Jin, C., Ward, M., & Done, C. 2012, MNRAS, 422, 3268
Kraft, R. P., Burrows, D. N., & Nousek, J. A. 1991, ApJ, 374, 344
Krolik, J. H., & Kallman, T. R. 1987, ApJL, 320, L5

LaMassa, S. M., Heckman, T. M., Ptak, A., et al. 2009, ApJ, 705, 568 (LM09)
LaMassa, S. M., Heckman, T. M., Ptak, A., et al. 2010, ApJ, 720, 786
LaMassa, S. M., Heckman, T. M., Ptak, A., et al. 2011, ApJ, 729, 52
Lamastra, A., Bianchi, S., Matt, G., et al. 2009, A&A, 504, 73 (L09)
Lavalley, M., Isobe, T., & Feigelson, E. 1992, in ASP Conf. Ser. 25, Astronomical Data Analysis Software and Systems I, ed. D. M. Worrall, C. Biemesderfer, & J. Barnes (San Francisco, CA: ASP), 245
Lawrence, A., & Elvis, M. 2010, ApJ, 714, 561
Liu, X., Zakamska, N. L., Greene, J. E., et al. 2009, ApJ, 702, 1098
Lusso, E., Comastri, A., Vignali, C., et al. 2010, A&A, 512, A34
Marconi, A., Risaliti, G., Gilli, R., et al. 2004, MNRAS, 351, 169
Melendez, M., Weaver, K. A., Mushotzky, R. F., et al. 2009, BAAS, 41, 239
Mulchaey, J. S., Koratkar, A., Ward, M. J., et al. 1994, ApJ, 436, 586
Nandra, K., Laird, E. S., Adelberger, K., et al. 2005, MNRAS, 356, 568
Panessa, F., Bassani, L., Cappi, M., et al. 2006, A&A, 455, 173
Piconcelli, E., Fiore, F., Nicastro, F., et al. 2007, A&A, 473, 85
Ptak, A., Heckman, T., Levenson, N. A., Weaver, K., & Strickland, D. 2003, ApJ, 592, 782
Ptak, A., Zakamska, N. L., Strauss, M. A., et al. 2006, ApJ, 637, 147 (P06)
Read, A. M., Rosen, S. R., Saxton, R. D., & Ramirez, J. 2011, A&A, 534, A34
Reyes, R., Zakamska, N. L., Strauss, M. A., et al. 2008, AJ, 136, 2373 (R08)
Rigby, J. R., Diamond-Stanic, A. M., & Aniano, G. 2009, ApJ, 700, 1878
Risaliti, G. 2002, A&A, 386, 379
Sazonov, S. Y., & Revnivtsev, M. G. 2004, A&A, 423, 469
Spergel, D. N., Verde, L., Peiris, H. V., et al. 2003, ApJS, 148, 175
Teng, S. H., Wilson, A. S., Veilleux, S., et al. 2005, ApJ, 633, 664
Treister, E., Krolik, J. H., & Dullemond, C. 2008, ApJ, 679, 140
Treister, E., & Urry, C. 2005, ApJ, 630, 115
Treister, E., & Urry, C. M. 2012, AdAst, 2012, 16
Trouille, L., & Barger, A. J. 2010, ApJ, 722, 212
Turner, T. J., George, I. M., Nandra, K., & Mushotzky, R. F. 1997, ApJS, 113, 23
Ueda, Y., Akiyama, M., Ohta, K., & Miyaji, T. 2003, ApJ, 598, 886
Vasudevan, R. V., & Fabian, A. C. 2007, MNRAS, 381, 1235
Vasudevan, R. V., Mushotzky, R. F., Winter, L. M., & Fabian, A. C. 2009, MNRAS, 399, 1553
Vignali, C., Alexander, D. M., & Comastri, A. 2004, MNRAS, 354, 720 (V04)

Vignali, C., Alexander, D. M., & Comastri, A. 2006, MNRAS, 373, 321 (V06)
Vignali, C., Alexander, D. M., Gilli, R., & Pozzi, F. 2010, MNRAS, 404, 48 (V10)
Vignali, C., Piconcelli, E., Lanzuisi, G., et al. 2011, MNRAS, 416, 2068
Xu, C., Livio, M., & Baum, S. 1999, AJ, 118, 1169
Yaqoob, T. 1997, ApJ, 479, 184
York, D. G., Adelman, J., Anderson, J. E., Jr., et al. 2000, AJ, 120, 1579

Zakamska, N. L., Gómez, L., Strauss, M. A., & Krolik, J. H. 2008, AJ, 136, 1607
Zakamska, N. L., Schmidt, G. D., Smith, P. S., et al. 2005, AJ, 129, 1212
Zakamska, N. L., Strauss, M. A., Heckman, T. M., Ivezić, Ž., & Krolik, J. H. 2004, AJ, 128, 1002
Zakamska, N. L., Strauss, M. A., Krolik, J. H., et al. 2003, AJ, 126, 2125 (Z03)
Zakamska, N. L., Strauss, M. A., Krolik, J. H., et al. 2006, AJ, 132, 1496